

MULTI-FREQUENCY IMPEDANCE CYTOMETRY FOR
BIOMOLECULAR SENSING AND CELL ANALYSIS

By

JIANYE SUI

A dissertation submitted to the

School of Graduate Studies

Rutgers, The State University of New Jersey

In partial fulfillment of the requirements

For the degree of

Doctor of Philosophy

Graduate Program in Electrical and Computer Engineering

Written under the direction of

Dr. Mehdi Javanmard

And approved by

New Brunswick, New Jersey

January, 2021

ABSTRACT OF THE DISSERTATION

Multi-frequency impedance cytometry for biomolecular sensing and cell analysis

By Jianye Sui

Dissertation Director: Dr. Mehdi Javanmard

We live in a world with persistent, emerging, and reemerging infectious disease threats. Infections can be caused by pathogenic microbes, including viruses, bacteria, fungi, and parasites. The detection and identification of these pathogens are critical for diagnosis and treatment. Electrical based biosensor is particularly attractive in recent years due to the ease of operation, rapid processing time, non-necessity of labeling, and the potential of miniaturization. Electrical impedance is a straightforward technique that could identify the presence of biomolecules and cells and enable quantification analysis. In this thesis, I developed an electrical impedance based platform to quantify DNA concentration for viral detection and measure the impedance signature of different phenotypes of microbes for classification and pathogen assessment.

For DNA quantification, we introduce the integration of paramagnetic beads with DNA fragments and apply a custom-made microfluidic chip to detect DNA molecules bound to beads by measuring impedance at multiple frequencies. Technical and analytical performance was evaluated using beads containing short oligonucleotides or

purified Polymerase Chain Reaction (PCR) products of different lengths and different concentrations.

Multiplex molecular biomarker analysis is of great importance in many biomedical and clinical studies. Electronic barcoding of micro-particles has the potential to enable multiplexing process. Nano-electronic barcoding works by depositing a thin layer of oxide on the top half of a micro-particle. We expanded library of nine barcoded particles by forming oxide layers of different thicknesses and different dielectric materials using atomic layer deposition and assess the ability to accurately classify particle barcodes using multi-frequency impedance cytometry in conjunction with supervised machine learning.

Separating specific cell phenotypes from a heterotypic mixture is a critical step in many research projects. Here we present the use of electrical impedance as an indicator of cell health and for identifying specific microbial phenotypes. We developed a microfluidic platform for measuring electrical impedance at different frequencies using *Staphylococcus aureus* and green alga *Picochlorum SE3*. Our results demonstrate the utility of electrical impedance as an indicator of cell phenotype by providing results that are consistent with known changes in cell size and physiology.

ACKNOWLEDGEMENT:

First, I would like to express my deep and sincere gratitude to my advisor Dr. Mehdi Javanmard for giving me an opportunity to do research and providing patient guidance and constant encouragement throughout this research.

Also, I am deeply thankful to all the committee members involved in the different stages of this dissertation — Dr. Curt Scharfe, Dr. Michael Wu, Dr. Umer Hassan, Dr. Yicheng Lu, and Dr. Leonard Feldman. I am incredibly grateful for their valuable advice and constructive suggestions for my research.

I would also like to acknowledge all of my collaborators. I want to thank Dr. Curt Scharfe and Dr. Neeru Gandotra for preparing DNA samples and providing insightful guidance. Thank Dr. Debashishi Bhattacharya and Dr. Fatima Foflonker for providing algae samples and helping interpret the results. Thank Dr. Jeffery Boyed and Dr. Hassan Al-Tameemi for culturing bacteria cells and giving helpful suggestions. Besides, I'd also like to thank Microelectronics Research Laboratory (MERL) at Rutgers University and The Center for Functional Nanomaterials (CFN) at Brookhaven National Laboratory for providing use of their equipment and materials for fabrication.

I extend my gratitude to the Electrical and Computer Engineering department at Rutgers University for providing me the opportunity to complete the Ph.D. program and I am grateful to all the staffs for their constant help.

Finally, I would like to express the deepest appreciation to my parents and my beloved friends, who provide me constant support and encouragement all through this time.

TABLE OF CONTENTS

ABSTRACT OF THE DISSERTATION	ii
ACKNOWLEDGEMENT:	iv
TABLE OF CONTENTS	v
LIST OF FIGURES	ix
Chapter 1: Introduction	1
1.1 DNA quantification and sizing.....	1
1.2 Multiplex biomarker analysis.....	3
1.3 Micro-algal cell health assessment.....	4
1.4 Bacterial phenotype characterization	6
Chapter 2: Multi-frequency impedance sensing for detection and sizing of DNA fragments	9
2.1. Introduction	9
2.2 Results	9
2.2.1 Device design	9
2.2.2 Electrical impedance sensing.....	11
2.2.3 DNA detection by impedance cytometry	14
2.2.4 Multi-frequency impedance response discriminates between different DNA sizes	19
2.3. Discussion and conclusion	21
2.4 Materials and Methods	25
2.4.1 Sample preparation	25

2.4.2 Electrode and microfluidic channel fabrication.....	26
2.4.3 Multi-frequency impedance flow cytometry	27
Chapter 3: Beadless DNA Assay for DNA sizing	29
3.1 Introduction	29
3.2 Methods and Materials	29
3.2.1 Electrode and microfluidic channel fabrication.....	29
3.2.2 Multi-frequency impedance measurement	30
3.3 Results and discussion.....	31
3.3.1 Multi-frequency impedance response of different lengths DNA samples .	31
3.3.2 Prediction of the DNA length based on the impedance.....	32
3.3.3 Comparison between bead-DNA assay and beadless DNA assay	33
Chapter 4: Electronic classification of barcoded particles for multiplexed	
detection using supervised machine learning analysis	35
4.1. Introduction	35
4.2. Methods and Materials	36
4.2.1 Barcoded particle fabrication.....	36
4.2.2 Sensor design and fabrication.....	37
4.2.3 Frequency-dependent impedance modulation	38
4.2.4 Multi-frequency impedance cytometry	39
4.2.5 Machine learning analysis	41
4.3. Results	41
4.3.1 Impedance response of particles at multiple frequencies	42
4.3.2 Effect of oxide layer thickness	43

4.3.3 Distinction between particles coated with different dielectric layers	47
4.4. Discussion	50
4.5. Conclusion.....	52
Chapter 5: Electrical impedance as an indicator of microalgal cell health.....	53
5.1. Introduction	53
5.2. Results	53
5.2.1 Microfluidic sensor design and electrical impedance analysis.....	53
5.2.2 Impedance analysis of algal cell viability.....	59
5.2.3 Algal cell stress analysis using impedance flow cytometry	61
5.3. Discussion and conclusion	66
5.4. Material and Methods.....	69
5.4.1 Algal cell preparation	69
5.4.2 Device fabrication and integration	69
5.4.3 Multi-frequency impedance flow cytometry	70
Chapter 6: Bacterial phenotype characterization based on electrical impedance signature.....	72
6.1 Introduction	72
6.2. Materials and Methods	72
6.2.1 Bacterial strains	72
6.2.2 Device fabrication and integration	73
6.2.3 Multi-frequency impedance flow cytometry	74
6.3 Results and discussions	74
6.3.1 Impedance analysis of bacterial cell viability.....	75

6.3.2 Bacterial phenotype characterization.....	76
Chapter 7: Conclusions	78
References:.....	82

LIST OF FIGURES

Figure 2-1. Device design. A) Image of the device B) The microscope image of channel and electrodes.	10
Figure 2-2. The schematic diagram of detection.	11
Figure 2-3. Representative data of bare paramagnetic beads passing through the sensing region measured at 7.5 MHz, 10 MHz, and 15 MHz respectively.	12
Figure 2-4. Impedance spectra of beads with different surface potential (M-270 and M-280).	14
Figure 2-5. Impedance spectra for beads attached with different concentrations of 300 bp ds DNA (Table 1) and negative control beads (paramagnetic M280, Invitrogen).	16
Figure 2-6. The quantification score of different 300 bp DNA beads and negative control was calculated based on impedance responses measured at 8 frequencies.	17
Figure 2-7. Impedance spectra for beads attached with different 157 bp ds DNA amount (0.039 fmol, 0.39 fmol and 0.74 fmol) and negative control (bare magnetic M280 beads).....	18
Figure 2-8. Quantification scores for beads attached with different 157 bp ds DNA amount (0.039 fmol, 0.39 fmol and 0.74 fmol) and negative control (bare magnetic M280 beads).....	19
Figure 2-9. Effect of different DNA lengths of the same concentration on impedance response. A) Impedance spectra of different length DNA beads. B) The quantification score of different length DNA beads.	21

Figure 2-10. The quantification score of different 300 bp DNA beads and negative control was calculated based on impedance responses measured at 7.5 MHz, 10 MHz, and 15 MHz.....	25
Figure 3-1 Impedance spectra of 209 bp and 358 bp DNA samples.	32
Figure 3-2. Confusion matrix of DNA length prediction	33
Figure 3-3. Quantification score of 209 bp and 538 bp DNA samples.....	34
Figure 4-1. Fabrication process of barcoded particles. A) Formation of self-assembled monolayer on glass by dip-coating glass slide. B) Deposition of oxide layer using atomic layer deposition (ALD). C) Re-suspension of particles to solution using ultrasonication.....	36
Figure 4-2. A) Schematic diagram of a multi-frequency impedance flow cytometer for classifying nanoelectronic barcoded particles. B) Image of the device.....	37
Figure 4-3. Schematic diagram of a multi-frequency impedance flow cytometer for classifying nanoelectronic barcoded particles.	40
Figure 4-4. Representative data of different beads passing through the sensing region measured at 7.5 MHz, 10 MHz, and 15 MHz respectively. A) Bare polystyrene beads B) Barcoded beads.	43
Figure 4-5. The impedance responses of barcoded particles with different thickness oxides. A) Scatter plot of peak amplitude @ 500 kHz vs. peak amplitude @ 15 MHz of particles with different alumina thickness. B) Scatter plot of peak amplitude @ 500 kHz vs. peak amplitude @ 5 MHz of particles with different hafnia thickness. C) Scatter plot of peak amplitude @ 500 kHz vs. peak amplitude @ 2 MHz of particles with different titania thickness.....	45

Figure 4-6. The accuracy of SVM model differentiating particles with different thickness of alumina.	46
Figure 4-7. The accuracy of the SVM model differentiating particles with different thickness of hafnia.	47
Figure 4-8. The impedance responses of barcoded particles with different dielectric oxides. A) Scatter plot of peak amplitude @ 500 kHz vs. peak amplitude @ 20 MHz for particles with 10 nm different oxides. B) Scatter plot of peak amplitude @ 500 kHz vs. peak amplitude @ 5 MHz for particles with 20 nm different oxides. C) Scatter plot of peak amplitude @ 500 kHz vs. peak amplitude @ 15 MHz for particles with 30 nm different oxides.	49
Figure 4-9. SVM results on differentiating barcoded particles with different dielectric oxides. A) The accuracy of SVM model differentiating particles with 10 nm different oxides. B) The accuracy of SVM model differentiating particles with 20 nm different oxides.	50
Figure 5-1. Microfluidic sensor. A) Image of the device whereby a soft-lithography made PDMS microfluidic channel is bound onto a glass wafer patterned with two pairs of sensing electrodes. B) Microscope image of the channel and electrodes.	55
Figure 5-2. Overview of strategy. A) Diagram showing the experimental design of the cell impedance experiments. B) Schematic diagram of the electrical impedance measurement.	56
Figure 5-3. Impedance response analysis. A) Representative data for algal cells flowing through the sensing electrodes, measured at 5 MHz, 7.5 MHz and 10 MHz. B) Impedance model of the cytometer system with the algal cell present.....	58

Figure 5-4. Impedance response of live and dead algal cells. A) Average cell transparency calculated using peak intensity measured at 20 MHz over peak intensity measured at 500 kHz. B) The impedance scatter of live and dead algal cells. C) Average impedance frequency response of live and dead algal cells.	60
Figure 5-5. Impact of different culture salt conditions on polystyrene bead (PS) and algal cell impedance. A) Average PS bead transparency calculated using peak intensity measured at 20 MHz over peak intensity measured at 500 kHz. B) Average cell transparency calculated using peak intensity measured at 20 MHz over peak intensity measured at 500 kHz.	62
Figure 5-6. Impact of time on algal cell impedance. The plot shows the average cell transparency calculated using peak intensity measured at 20 MHz over peak intensity measured at 500 kHz.	64
Figure 5-7. The impedance scatter of individual algal cells cultured in different salinity media for 1h (a), 5h (b), 1d (c), and 5d (d).	65
Figure 6-1. Impedance spectra of alive and dead cells. The impedance was measured at 500 kHz, 2 MHz, 5 MHz, and 7.5 MHz. The dot line shows the trend of impedance change as frequency increases.	76
Figure 6-2. Impedance spectra of different phenotypic bacteria (Wild type, HemB mutant and MenD mutant). The impedance was measured at 500 kHz, 2 MHz, 5 MHz, and 7.5 MHz. The dot line shows the trend of impedance change as frequency increases.	77

Chapter 1: Introduction

This chapter gives an overview of the research proposal concepts and problem statements for DNA quantification and sizing, biomarker multiplex analysis, microalgal cell health assessment, and bacterial phenotype characterization. It briefly explains the background of each part of project and clarifies why these issues are worthy to attention nowadays.

1.1 DNA quantification and sizing

Miniaturized technologies for quantification and sizing of nucleic acids can serve as point-of-use tools for research and clinical applications ranging from infectious and genetic disease testing to screening of environmental samples for viral and pathogen detection [1, 2]. Gold standard techniques for highly sensitive DNA quantification are optical in nature and generally require bulky instrumentation for readout, such as fluorescence [3-5] and plasmonic based detection [6-8]. Optical imaging technologies have been miniaturized to detect fluorophores for on-chip optofluidic microscopy [9, 10], portable tomographic microscopy [11] and cell-phone based microscopy [12, 13]. More recently, the use of deep-learning in conjunction with cell-phone microscopy has enabled development of portable tools for analyzing nucleic acids [14]. Though much progress has been made in building portable optical systems, ultra-compact portable [15-18] and wearable [19, 20] devices can be more readily achieved by using electrical biosensors due to the comparative ease in miniaturizing electronic systems.

Electrochemical quantification of DNA typically relies on the addition of a redox probe molecule [21, 22] or an enzymatic reaction [23] as implemented using screen-printed electrodes, carbon nanotubes, conductive polymers, and gold nanoparticles on complementary metal-oxide-semiconductor (CMOS) substrates [24-27]. Prior work with graphene-based electrodes for nucleic acid quantification has relied on the electron transfer properties of the nucleic acids themselves [28, 29]. Electronic flow-through measurements (e.g., impedance cytometry, nanopores) detect and quantify analytes (cells, particles, molecules) passing through a micro- or nanoscale aperture based on real-time monitoring of direct changes in electrical properties such as impedance, resistance/conductance, charge, or other dielectric properties [30-33]. Recently, tunable resistive pulse sensing was used to measure surface (Zeta) potential of paramagnetic beads coated with DNA [34]. A variety of nanopore based geometries have been utilized for quantifying and sizing of nucleic acids strands based on measurable differences in electric current during DNA translocation across nanopores [35, 36]. While highly sensitive, the precise manufacturing of nanoscale pores with high-yield and robust operation resilient to clogging and device failure still remains a challenge [37]. Instead of using nanopores, L. Esfandiari et al. achieved sequence-specific DNA detection by investigating the blocked current of the bead hybridizing with a target DNA [38]. Previously, Saleh, Sohn et al. reported the use of resistive pulse sensing across microscale pores for protein detection [39], where quantification relied on the use of target antigen binding to antibody coated colloids, and detecting changes in DC current across pores as a result of binding. However, the use of this technique for consistent and repeatable detection and quantification of nucleic acid strands with DC

or low-frequency (<100 kHz) is challenging, particularly for shorter DNA strands (<100 bp).

1.2 Multiplex biomarker analysis

Biomarker-based analysis has the potential to enable early disease diagnosis, prognosis, health monitoring, therapy management, and also drug toxicity [40-43]. Given the heterogeneity across the population in various disease conditions, the analysis of a multitude of biomarkers using multiplexing technologies is necessary for improving sensitivity and selectivity of diagnosis [44-46].

Two general modalities available for detection of biomarkers include optical and electrical detection. Optical detection technologies are typically more sensitive by nature compared to their electrical counterparts and have enabled high throughput multiplexing through use of various barcoding methods, however, the instrumentation tends to have a large footprint, thus more suitable for benchtop applications [47-50]. Common techniques used for particle barcoding include photo-patterning [51, 52], the use of fluorescent colloids [53, 54], and semiconductor quantum dots [55-58]. These technologies have been demonstrated for multiplex analysis of nucleic acids [59] and proteins [60]. The Luminex platform is a commercially available benchtop instrument for high-throughput multiplexed biomarker analysis which uses two-photon excitation of fluorescent magnetic microspheres [61, 62].

On the other hand, electrical impedance and electrochemical-based techniques are usually low cost, low power, lightweight, and easy to miniaturize. While various electrical technologies have been developed capable of highly sensitive biomarker

analysis [32, 63, 64], however, they have lagged behind their optical counterparts in terms of throughput due to the lack of suitable methods for barcoding particles. The most straight forward method for impedance based multiplex analysis would involve utilization of beads of different sizes, however variations in fabrication, along with bead aggregation would limit the ultimate throughput. Previously, we (Xie et al.) presented a new impedance based barcoding approach that deposits tunable nano-capacitors on the surfaces of microsphere, thus enabling miniaturization of the readout instrumentation [65]. The nano-capacitor consisted of an electron beam evaporated gold layer on the top half of the sphere, and with another atomic layer deposited oxide layer on top, forming a Janus particle. These barcodes utilize a well-known, but previously unexplored phenomenon of Janus particles that the Clausius-Mossotti (CM) factor spectrum shifts depending on the zeta potential of the dielectric half of the microsphere, and also the fact that the CM factor can be obtained directly by measuring the frequency dependent impedance for each particle.

1.3 Micro-algal cell health assessment

An important branch of functional genomics relies on the bioinformatic analysis of bulk transcriptomic data (e.g., RNA-seq reads from Illumina or Iso-Seq data from PacBio platforms) to identify pathways involved in processes such as the cell cycle, stress and disease response, and development [66-68]. Although well understood and relatively easy to apply, these methods are nonetheless expensive and provide average gene expression data based on the analysis of millions of cells per sample. To achieve single-cell resolution of gene expression patterns requires the more specialized tools of single

cell transcriptomics that may be limited to smaller sample sizes due to the costs of generating individual libraries for 100s or 1000s of cells, followed by high-throughput sequencing [69, 70]. Given these considerations, there is a need to develop tools with single cell resolution that provide meaningful insights into cell health and can be applied to millions of cells at low cost. If such an approach does not require existing reference genome data (preferable for RNA-seq approaches), then it can be applied to a variety of non-model systems (algal or microbial) that are of high importance in natural settings. Such a tool should be portable and its use not limited to laboratories or highly trained specialists. Here we describe a microfluidic platform for measuring cell health at the single cell level that addresses many of the shortcomings of conventional approaches.

Our approach builds on the growing interest in electrical analysis of biological cells. Particularly attractive is the ease of operation, rapid processing time, non-necessity of labeling, and the potential of miniaturization of these methods. For these reasons, electrical properties of cells have been investigated and utilized in a broad array of fields such as disease diagnosis [18, 37, 71, 72], environmental monitoring [73, 74], food safety [75], and in applications such as cell identification and separation [76-78]. Specifically, electrical impedance spectroscopy has been used to analyze cell electrical properties [20, 79-82]. Impedance measurement is based on the changes in conductivity and permittivity in a medium due to the presence of cells. Electrical impedance measured at different frequencies provides different types of information about cells, including cell size and membrane and cytoplasm electrical properties [83]. Impedance indicates cell size at lower frequencies around several hundred kilohertz, whereas it can

be used to interpret membrane reactance and cytoplasm conductance at higher frequencies [83, 84]. With the aid of microfluidic flow cytometry technology, impedance spectroscopy requires a smaller sample volume when compared to traditional methods, while maintaining high sensitivity [85-87]. Moreover, it simplifies the preparation process that may alter cell properties during the sorting step. Morgan's group used microfluidic impedance cytometry to discriminate T-lymphocytes, monocytes, and neutrophils in blood with high accuracy [88]. Based on the electrical impedance, cells with particular properties can be sorted for downstream analysis. Haandbæk and co-authors reported a cytometer with the capability of wide frequency range measurement and characterized two different types of yeast cells based on dielectric properties at four frequencies [89]. There are some known connections between electrical properties of cells and their biological status, such as viability. Song et al. differentiated live and dead *Dunaliella salina* cells with a capacitive microfluidic sensor [90]. In spite of these promising results, the use of electrical impedance for cell health screening is poorly developed.

1.4 Bacterial phenotype characterization

In recent years, the rising antimicrobial resistance has become a looming threat for us all over the world. It nullifies the effect of antimicrobial drugs and results in the drug becoming ineffective. The consequence could be as bad as 10M death per year by 2050 if we don't address the problem properly [91]. Antimicrobial resistance is a natural phenomenon in bacteria. However, the use of antibiotics prompts the selection process that the bacteria with antimicrobial resistance can survive and even multiply. The

inappropriate use of antibiotics makes this situation even worse [92]. Therefore, bacterial phenotype characterization and antimicrobial susceptibility tests (AST) is crucial for infection diagnosis and treatment.

Genotypic tests and phenotypic tests are the two main categories of conventional approaches for testing antimicrobial susceptibility. The genotypic test relies on the detection of the specific resistance gene. Polymerase chain reaction (PCR) is the most commonly used nucleic acid amplification technique and has been widely adopted in the genotypic test [93, 94]. Benefiting from monitoring the amplified product during amplification, real-time PCR has been more involved in the genotypic test in recent years [95, 96]. It is more sensitive and reproducible while minimizing carryover contamination. However, these tests are expensive and limited to the known genes. Moreover, the presence or absence of a gene does not correlate with phenotypic susceptibility all the time. The difference in gene expression level and the complicated mechanisms to achieve antimicrobial resistance are challenges for the genotypic test.

The phenotypic test evaluates the antimicrobial resistance based on the viability or growth response of a microbe in the presence of an antibiotic. It's the standard method used in microbiology labs [97]. Broth dilution tests and disk diffusion tests are two commonly performed phenotypic tests. Broth dilution test determines the susceptibility in terms of the minimal inhibitory concentration (MIC), which is the lowest concentration of antibiotic that prevented growth. While, dilution test provides qualitative susceptibility results (i.e., susceptible, intermediate, or resistant) by measuring the diameter of the zone of growth inhibition. Although these techniques are the most commonly used methods for AST, they generally need a long incubation time

around 16–24 h. Recently, some automated AST platforms take advantage of sensitive optical detection readers to detect microbial growth and provide faster results (3.5–16 h) [97, 98]. A rapid AST that provides a susceptibility profile within a short period could enable more timely changes to appropriate antimicrobial treatments [99].

Chapter 2: Multi-frequency impedance sensing for detection and sizing of DNA fragments

2.1. Introduction

In this project, we introduce a novel approach to identify DNA fragments based on their frequency-dependent dielectric properties. We use multi-frequency excitation of electric fields within a small microfluidic PDMS channel to detect changes in electrical impedance as DNA fragments, which are coupled on micron-sized particles, pass through the channel. By combining PCR-based amplification with electrical detection, non-target sequences are removed prior detection in order to maximize the precision and accuracy for DNA target analysis. To investigate the capability of this technology to distinguish DNA fragments of different quantity and size at high sensitivity, we studied the effect of different DNA concentrations and fragment lengths on frequency-dependent electrical impedance changes. We show that this electronic biosensor could be used to rapidly detect and size DNA fragments at the femtomole level over a 100-fold dynamic range.

2.2 Results

2.2.1 Device design

Our device is designed to perform multi-frequency impedance cytometry for direct detection of DNA captured on paramagnetic beads. The basic device consists of two layers covalently bonded together. The first layer is a microfluidic channel made of

polydimethylsiloxane (PDMS), and the second layer is a pair of electron beam-deposited reusable coplanar gold electrodes on a fused silica substrate (Figure 2-1 A and B). Each electrode is 20 μm wide and the gap between the two electrodes is 30 μm . The sensitivity of the detector increases as the diameter of the channel approaches the size of the bead, while in turn the risk of clogging significantly increases as the channel becomes too small. The micro-channel was designed with the dimension of 30 μm in width and 15 μm in height, which is large enough to minimize clogging and small enough to obtain sufficient sensitivity during measurements.

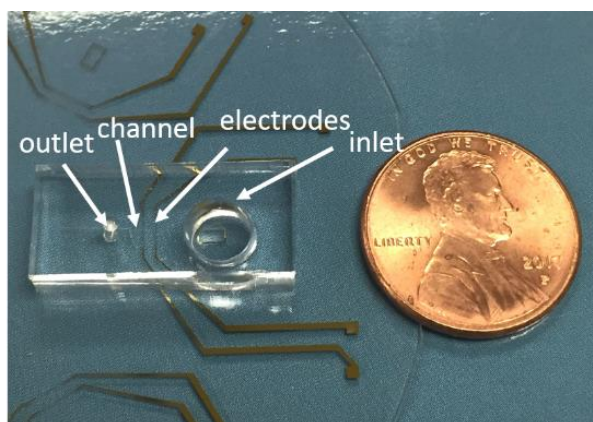
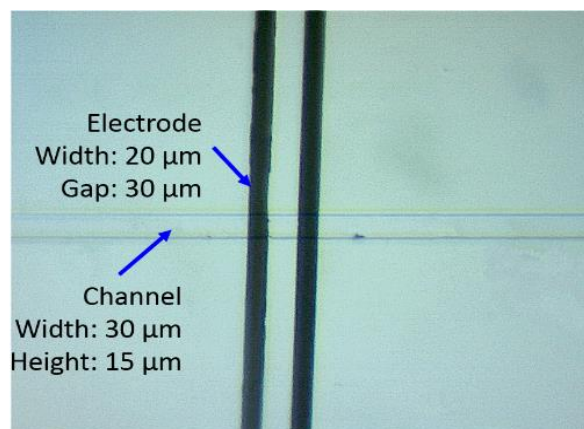
A**B**

Figure 2-1. Device design. A) Image of the device B) The microscope image of channel and electrodes.

2.2.2 Electrical impedance sensing

We performed multi-frequency impedance cytometry to detect the impedance difference of beads coupled with different DNA amounts. When a bead flows through the sensing region, it partially impedes the AC electric field generated between the two electrodes, which results in an instantaneous frequency-dependent drop in ionic current, i.e., a momentary increase in impedance. Using a multi-frequency lock-in amplifier (Zurich Instruments HF2A, Zurich, Switzerland), the impedance response was measured simultaneously at 8 different frequencies ranging from 100 kHz to 20 MHz. One electrode was excited with a combination of 8 different frequency AC signals and the other electrode was tied to a transimpedance amplifier (Figure 2-2).

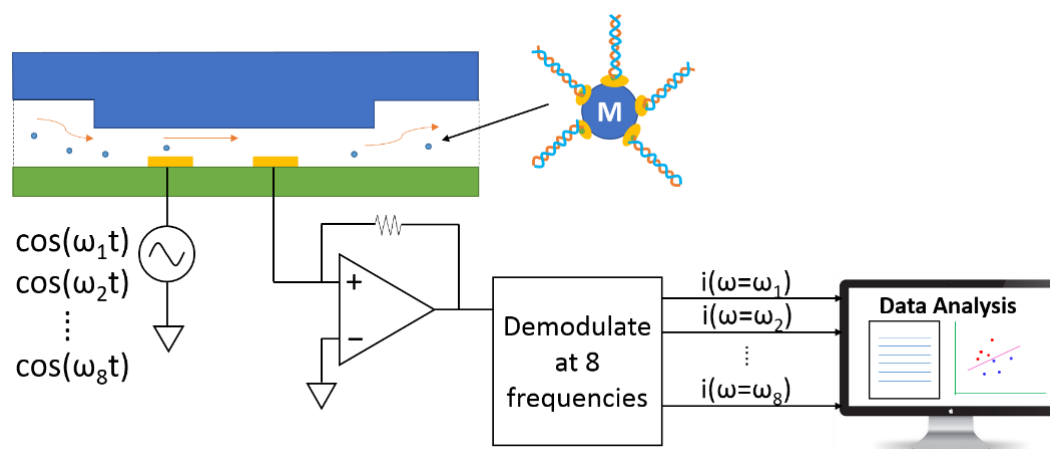


Figure 2-2. The schematic diagram of detection. The bead is injected from inlet well using micro pipette. As beads flow through the pore, the impedance change is captured by the lock-in amplifier at multiple frequencies. The data are sent to the PC and analyzed in Matlab.

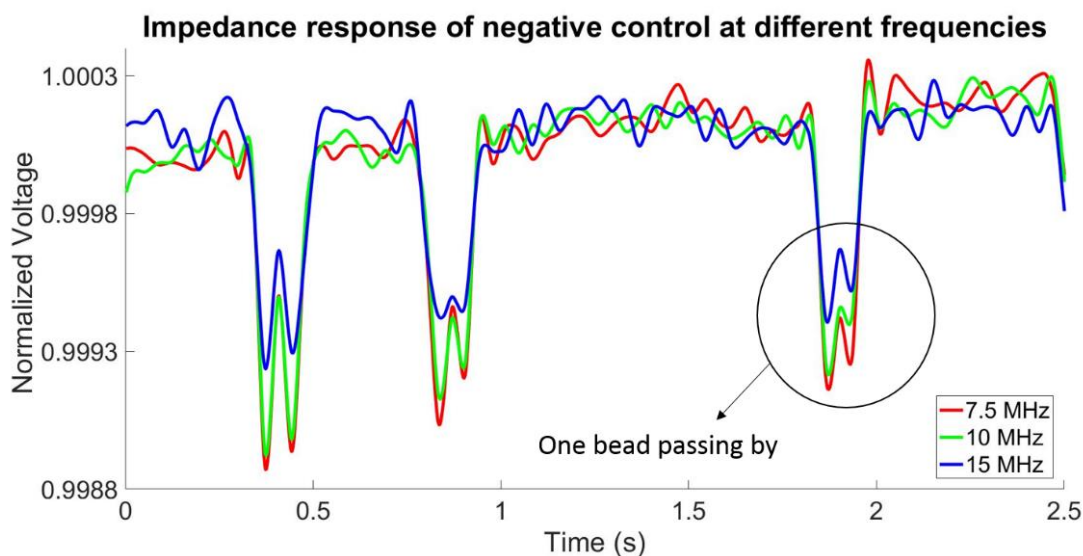


Figure 2-3. Representative data of bare paramagnetic beads passing through the sensing region measured at 7.5 MHz, 10 MHz, and 15 MHz respectively.

Different quantities and sizes of DNA immobilized onto paramagnetic beads not only modulate the overall diameter of the DNA beads as compared to bare beads, but also influence surface potential, conductance, and permittivity. Each of these physical parameters was associated with differences in impedance measurements at different frequencies. Figure 2-3 shows the representative multi-frequency (7.5 MHz, 10 MHz and 15 MHz) time series data of bare paramagnetic beads in a 2.5s time window. Traces are normalized with respect to the baseline impedance for ease of comparison. Each double peak observed corresponds to a single bead passing over the two electrodes. The reason for the double peak is due to the fact that when a bead flows directly above one electrode, a relative larger perturbation to the electric field is created compared to the bead flowing through the space between the two electrodes, thus resulting in two smaller peaks superimposed on a large peak. The bead can be modeled as a capacitor

and a resistor in series with each other, which is parallel to the resistance of the solution. As frequency increases greater than 5 MHz, the impedance decreases due to the parasitic capacitance, which creates a path for the electric field parallel to the conductive solution, thus making the beads more permeable to the electric field generated by the electrodes. The impedance difference between beads containing DNA compared to bare beads without DNA was significantly larger at higher frequencies (> 500 kHz), due to the dominance of surface potential, conductance, and permittivity in impedance, as opposed to lower frequencies where impedance peak response (IPR) was primarily dictated by bead diameter. The summing of peak intensities of each bead across the frequency spectrum enabled maximum differentiation between different bead populations. To determine the dominant physical mechanism that allows for bead differentiation in the frequency region of interest, we performed measurements on beads of the same size but with differing surface potentials (Figure 2-4). Beads with larger surface potential displayed a higher average distribution of IPR, suggesting that the dominant mechanism for DNA detection was a change in surface potential. Previous work [39] involving DC current measurements relied on changes in diameter.

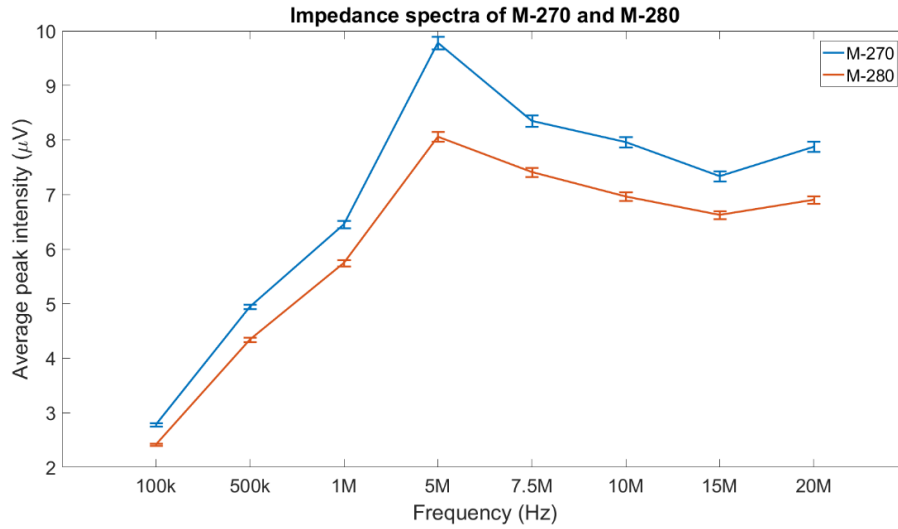


Figure 2-4. Impedance spectra of beads with different surface potential (M-270 and M-280).

2.2.3 DNA detection by impedance cytometry

Testing of 300 bp DNA beads

Measurements of beads with different DNA concentrations were performed to study the effect of different DNA amounts on frequency-dependent impedance sensing. A stock solution of beads coated with 300bp DNA fragments was prepared of which only a small sample amount was used for impedance cytometry (Table 1). The current design of the device requires a minimum volume to maintain free flow in the PDMS microfluidics channel. In order to test the sensitivity of the device for detecting small DNA amounts, a one microliter aliquot of the DNA coated beads was diluted in 60 μ L of phosphate buffered saline (PBS). Due to its relatively high salt concentration and increased conductivity, PBS has been shown to increase the sensitivity in impedance measurements [100].

Table 2-1. DNA samples analyzed

DNA length	DNA copies per bead	DNA amount per bead (ng)	Measured DNA amount^ (ng)	Measured DNA concentration^ (fmol)
613bp*	4.75×10^5	3.15×10^{-4}	0.1575	0.39
300bp*	4.75×10^5	1.54×10^{-4}	0.077	0.39
300bp	2.37×10^5	7.69×10^{-5}	0.03845	0.19
300bp	4.75×10^4	1.54×10^{-5}	0.0077	0.039
300bp	4.75×10^3	1.54×10^{-6}	0.00077	0.0039
300bp	4.75×10^2	1.54×10^{-7}	0.000077	0.00039
300bp	4.75×10^1	1.54×10^{-8}	0.0000077	0.000039
157bp	9.08×10^5	1.54×10^{-4}	0.077	0.74
157bp*	4.75×10^5	8.05×10^{-5}	0.04025	0.39
157bp	4.75×10^4	8.05×10^{-6}	0.004025	0.039

* 3 samples selected to study the effect of DNA length on impedance response (see Figure 2-4)

^ For each sample, measurements were performed using an aliquot of approximately 500 beads.

Figure 2-5 shows the impedance spectra of beads with different DNA amounts measured at 8 frequencies. For each of the DNA concentrations measured, the average IPR gradually increased in value from 100 kHz to 5 MHz and decreased in value from 7 to 15 MHz. There was a positive correlation between DNA amounts and average IPR. At higher frequencies, the IPR of the negative control (bare streptavidin-coated paramagnetic beads) overlapped with that of beads with low DNA amounts. These findings showed the positive correlation of DNA amounts attached to beads with IPR. We observed a linear increase in average IPR for DNA concentrations up to 0.19 fmol.

Increased DNA amounts resulted in a higher surface potential of the beads, which was associated with a larger impedance difference compared to control bare bead.

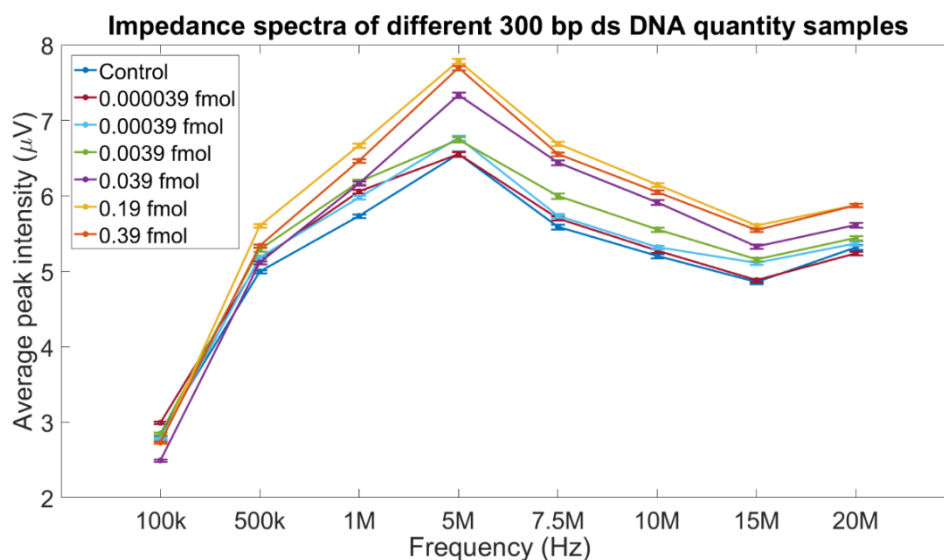


Figure 2-5. Impedance spectra for beads attached with different concentrations of 300 bp ds DNA (Table 1) and negative control beads (paramagnetic M280, Invitrogen).

DNA Quantification Score

To quantify DNA fragment amounts and distinguish samples with different DNA concentrations, we developed a quantification score (Q-score) combining data from eight frequency measurements. For each sample, we averaged the IPR of each bead measured at the eight frequencies. To account for device-to-device variation and day-to-day environmental variation (e.g., room temperature, humidity) which could potentially affect the impedance response, DNA sample beads were always analyzed in comparison to bare beads measured in the same experiment. This allowed for calibrating IPR of DNA coated beads with bare beads to account for possible variations. As the DNA amount on beads increased, the difference in Q-score between DNA beads

and bare paramagnetic beads increased. We studied the linear correlation between quantification score and the logarithm of DNA quantity attached to the beads. Figure 2-6 shows the Q-score of beads with differing DNA concentrations compared to bare streptavidin coated paramagnetic beads. Results showed approximately two orders of magnitude dynamic range with a detection limit of 0.0039 fmol (quantity of DNA in measured 500 beads) for 300 bp DNA strands ($p < 0.001$), which was the equivalent to 1.54 fg per bead. The curve was flat below the detection limit because the DNA was no longer detectable. The high end of the linear dynamic range was 0.19 fmol as increased DNA sample concentration was not able to further increase the bead's surface charge and IPR. Duplicate experiments were performed on the same device to validate results.

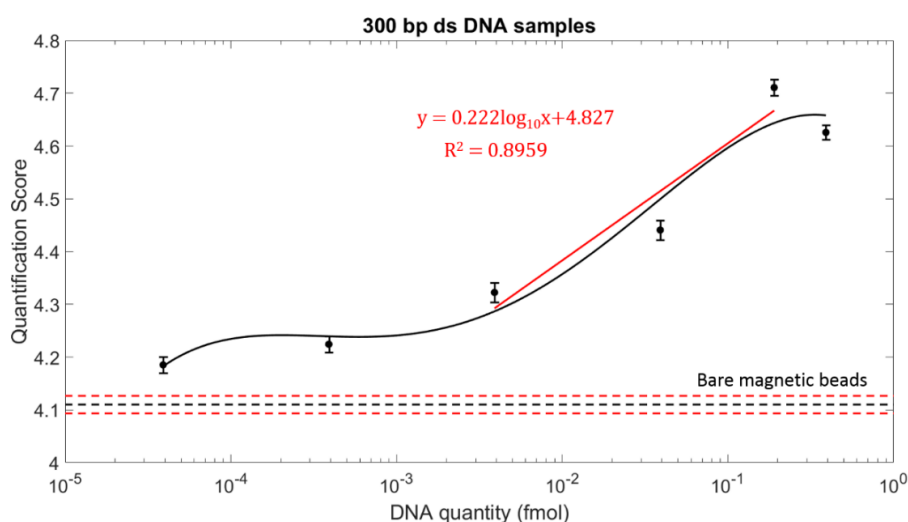


Figure 2-6. The quantification score of different 300 bp DNA beads and negative control was calculated based on impedance responses measured at 8 frequencies. The black solid line shows the polynomial fitted curve across the different DNA concentrations. The red line shows the linear correlations between DNA quantity and quantification score in the linear region. Error bars represent standard error of mean. Horizontal black and red dotted lines represent the average quantification score of the negative control samples and negative control \pm standard error, respectively.

Testing of 157 bp DNA beads

We also measured DNA amounts for beads containing 157 bp double-stranded PCR products (Table 1). The IPR for these samples showed responses similar to those of the 300 bp DNA samples (Figure 2-7) with a detection limit of 0.039 fmol. The Q-score plot is shown in Figure 2-8. The R^2 values indicated the linearity between two parameters (Q-score and nucleic acid quantity). The average Q-score of 0.039 fmol 157 bp DNA samples was at least one standard error above the upper bound (standard error) of the average Q-score of DNA-free control samples.

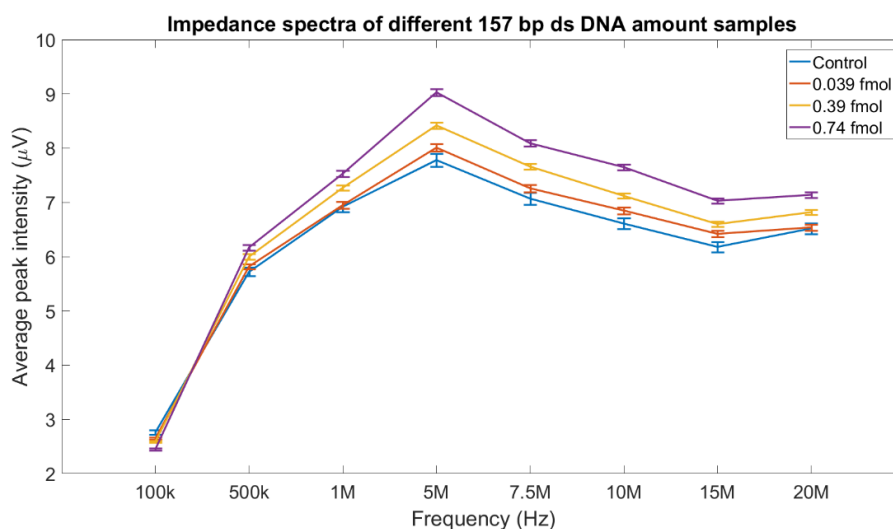


Figure 2-7. Impedance spectra for beads attached with different 157 bp ds DNA amount (0.039 fmol, 0.39 fmol and 0.74 fmol) and negative control (bare magnetic M280 beads).

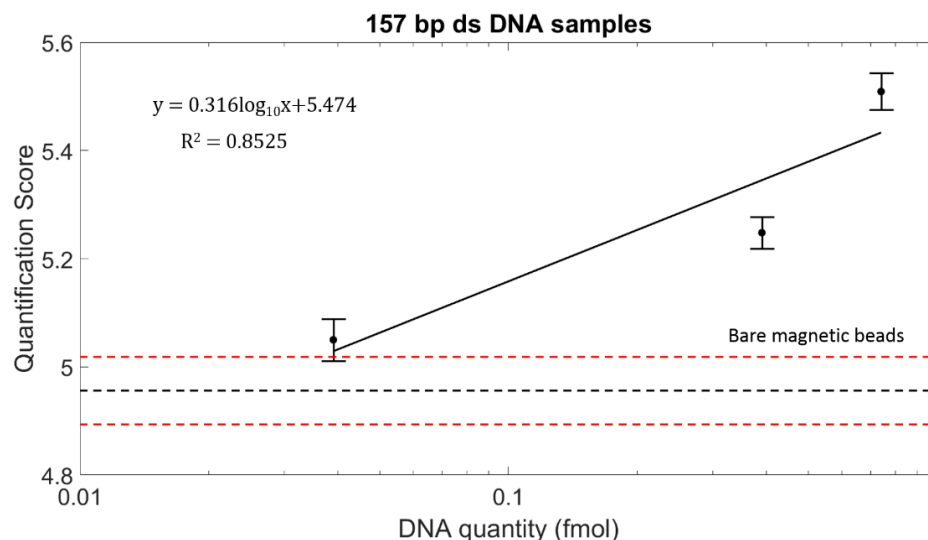


Figure 2-8. Quantification scores for beads attached with different 157 bp ds DNA amount (0.039 fmol, 0.39 fmol and 0.74 fmol) and negative control (bare magnetic M280 beads). Linear correlations between quantification score and the logarithm of 157 bp DNA fragments attached to the beads were calculated. Error bars represent standard error of mean. Horizontal black and red dotted lines represent the average quantification score of the negative control samples and negative control \pm standard error, respectively.

These results demonstrated our device's capability of quantifying DNA concentration based on multi-frequency impedance information. The results also illustrated that the detection limit of DNA concentration was length-sensitive. In addition to detecting PCR products of different lengths, we demonstrated the ability of our device for electronical detection of 30 base oligonucleotides with respective IPR responses and Q-score plots.

2.2.4 Multi-frequency impedance response discriminates between different DNA sizes

We investigated if the length of DNA fragments attached to beads could have an effect on electrical impedance. Average IPR was calculated by measuring the impedance of beads containing DNA fragments of different length but of the same molar concentration at eight different frequencies (Figure 2-9). The 613 bp DNA beads had the largest relative IPR for all frequencies tested, while beads coupled with 157 bp DNA had the smallest IPR. We also used the Q-score to identify the impedance difference between DNA beads and the negative control across all frequency measurements. As shown in Figure 8B, the Q-score increased linearly with increasing DNA length. Since the number of copies per bead was identical for all samples, beads coated with longer DNA fragments showed a higher electrical surface potential and thus a higher average IPR. The average Q-score for 157 bp beads at 0.39 fmol was at least one standard error above the upper bound (standard error) of the average Q-score of DNA-free control beads.

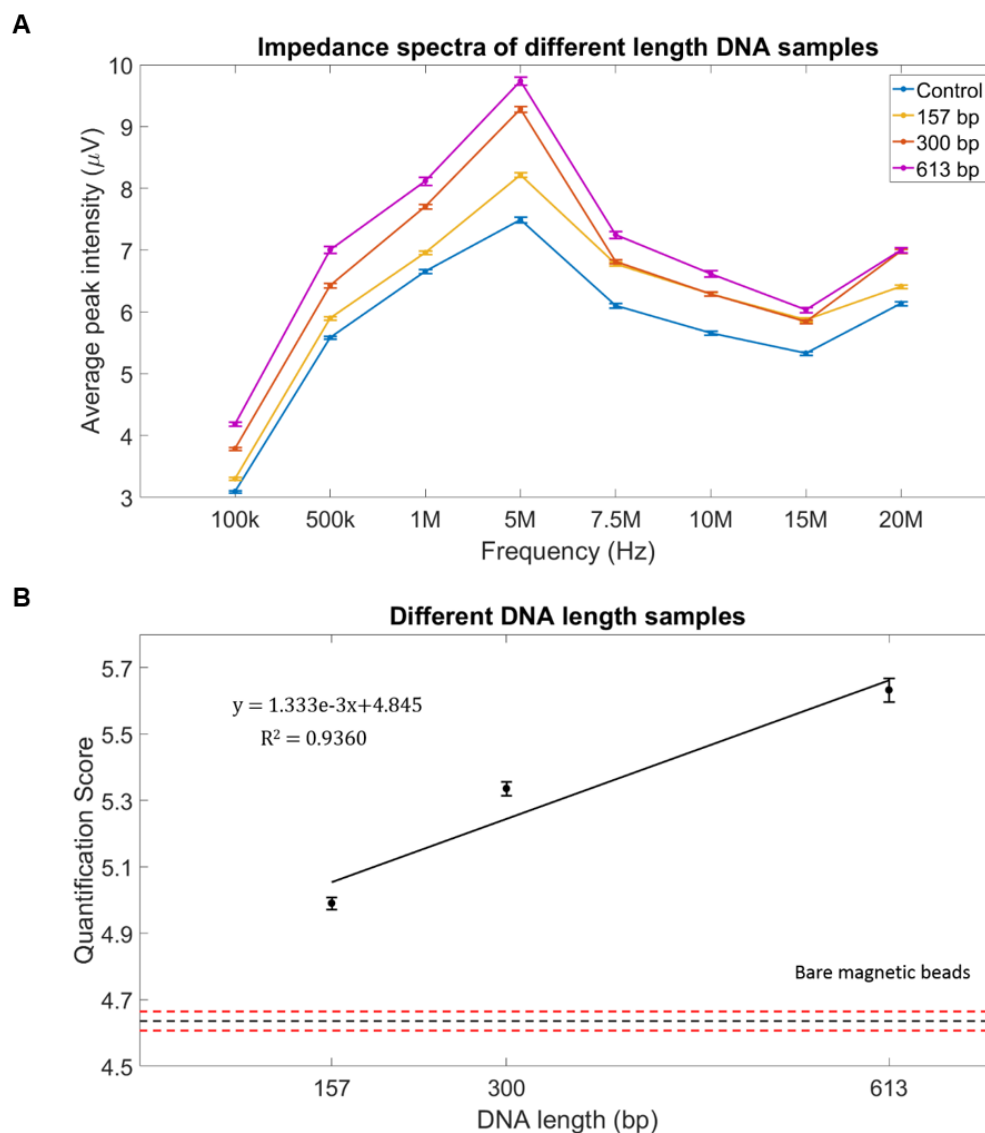


Figure 2-9. Effect of different DNA lengths of the same concentration on impedance response. A) Impedance spectra of different length DNA beads. B) The quantification score of different length DNA beads.

2.3. Discussion and conclusion

In this work, we present a novel method for electronic detection and sizing of DNA fragments coupled onto paramagnetic beads using multi-frequency impedance cytometry. Our technology improves on previous electronic techniques that relied on

particle diameter [39, 101-104] by capturing additional frequency-dependent properties such as surface potential and conductivity changes. We show that DNA binding changes the surface potential of paramagnetic beads, which can be detected through frequency-dependent impedance peak response. IPR differed between DNA coated beads and bare streptavidin coated beads (negative control) as DNA concentration increased in the linear region of the dynamic range. We show the utility of this new technology for reliable detection of DNA fragments of different concentrations and lengths. This technology has potentially broader applications for detection and quantification of nucleic acid including mRNA and microRNA.

Starting from a genomic DNA sample, targeted PCR amplification of specific genomic regions is performed to reduce sample complexity and increase sensitivity and specificity for target detection. The coupling of DNA fragments to beads increases the relative impedance changes for DNA detection. The biotinylated DNA strands are easily captured onto streptavidin coated beads, and in combination with impedance flow cytometry, hundreds of beads can be continuously detected within minutes for rapid and highly sensitive DNA detection. This method requires only a small sample volume, which could be further reduced by technical optimization of the device. Given that DNA fragments are immobilized on beads instead of on the surface of the microfluidics channel, this technology is reusable and potentially portable. In future work, we envision utilizing barcoded beads, each carrying either a different length product or different target to perform multiplex analysis [65, 105].

Currently, gel electrophoresis and real-time PCR are widely used in DNA quantification and sizing. Using optimized gel electrophoresis technology, Agilent

Bioanalyzer can detect PCR products with a concentration as low as 0.1 ng within an analysis time of 30 minutes. In comparison, Real-Time PCR utilizes optical instrumentation and has a detection limit of several copies/ μL or several fg/ μL . While highly sensitive, real-time PCR has limitations in terms of DNA fragment size (e.g. amplicon size should be < 200 bp) and limited multiplexing capabilities. Our impedance sensor in combination with microfluidics technology could potentially be designed for multiplex and portable applications, however, more work is needed to show technical and analytical feasibility for this approach. To further advance the technology towards clinical translation, several technical optimizations can be made to minimize device to device variations. These include incorporation of multiple electrodes for redundancy of measurements as well as temperature sensors to assess and correct for day-to-day variations. These improvements could result in further reduction of the number of beads required for accurate DNA detection, which could lower the limit of detection and further decrease analysis time. We found that 150 beads (Q-score of 4.32, $p < 0.05$) randomly selected from the approximately 500 beads measured per experiment was sufficient to distinguish beads containing DNA fragments from negative control beads. Another technical optimization could be the use of pulseless and noiseless pressure pumps that could help decrease the required sample volume and measurement time. We estimated the flow rate in the PDMS microfluidics channel at $0.05 \mu\text{L}/\text{min}$ by comparing to experiments performed using a syringe pump. Thus, less than $1 \mu\text{L}$ of sample was used for measurement in the experiment while the remaining $59 \mu\text{L}$ were used for maintaining the flow. These results indicate that measurements using this device could potentially be performed

using much smaller DNA input amounts and in even shorter time. Importantly, clinical validation of this device will require establishing DNA standards with known concentration and length. These standards would be run together with every test sample taking advantage of the technique's strength in making multiple relative measurements. Our experiments provide an approach to establish such standards and to quantify DNA fragments at high accuracy and precision at the femtomolar level and over a 100-fold dynamic range.

The detection limit does not necessarily decrease as the number of frequencies used increases, since the impedance responses are not always separable at all eight frequencies. By looking at several specific frequencies, we could achieve an even lower detection limit. As shown in Figure 2-5, the impedance responses are more distinct at 7.5 MHz, 10 MHz, and 15 MHz. If modifying the definition of the quantification score to the summation of the peak amplitude measured at these three frequencies, we could observe a broader linear dynamic range (from 0.000039 fmol to 0.19 fmol), as shown in Figure 2-10. The detection limit further decreases to 0.000039 fmol, the quantification score of which is still higher than the negative control. The linear correlation between the quantification score and the logarithm of the DNA quantity attached to the beads was studied. An R-squared value of 0.9203 was achieved.

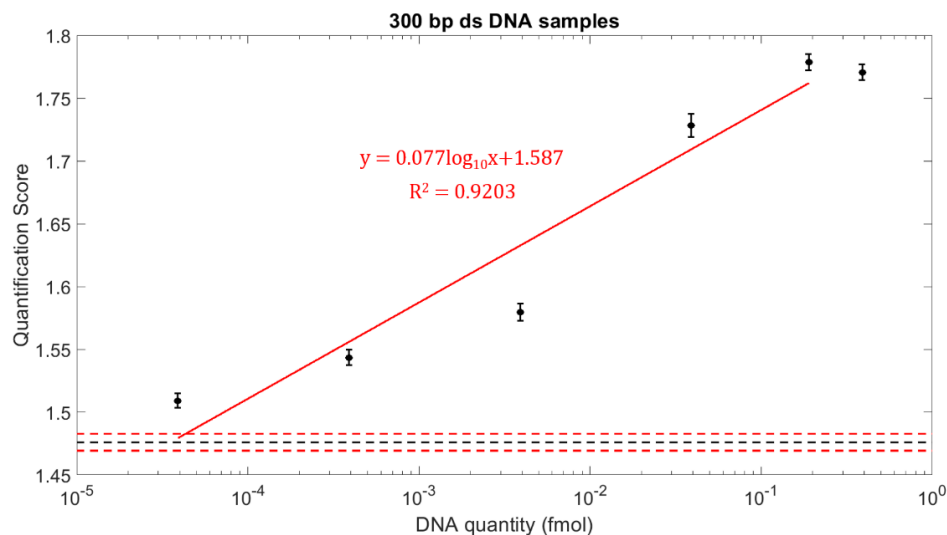


Figure 2-10. The quantification score of different 300 bp DNA beads and negative control was calculated based on impedance responses measured at 7.5 MHz, 10 MHz, and 15 MHz.

2.4 Materials and Methods

2.4.1 Sample preparation

Target DNA was generated using biotinylated DNA oligonucleotides and Polymerase Chain Reaction (PCR). The purified DNA fragments were coupled to 2.8 μm bare paramagnetic beads via streptavidin-biotin linkage (Fig. 1C) using the procedure detailed as follows. Biotinylated oligos synthesized by IDT (Coralville, IA, USA) were used to amplify different fragment sizes (157bp, 300bp, 613bp) of mitochondrial DNA under standard PCR conditions. The PCR product was purified using Qiaquick PCR purification kit (Qiagen) to remove any unincorporated biotinylated oligos. The PCR product was eluted in water, quantified and prepared for immobilization to the streptavidin coated dynabeads (M280) from Invitrogen (11205D). The dynabeads were

washed as per the manufacturer's recommendations. The washed beads were then immobilized with the purified biotinylated DNA and incubated at room temperature for 15 min using gentle rotation at 2000 rpm. Different concentrations of DNA were bound to the paramagnetic beads (Table 1). The biotinylated DNA coated beads were then separated on a magnet for 2-3 min and subsequently washed 2-3 times as per manufacturer's recommendations. Finally, the washed biotinylated DNA coated beads were resuspended in 10 μ l of water, for final concentrations as listed in Table 1. A separate set of samples was generated for beads with similar DNA copy numbers for ss 30 base, ds 157 bp, ds 300 bp and ds 613 bp fragments.

2.4.2 Electrode and microfluidic channel fabrication

We used standard photolithography, electron beam evaporation, and lift-off processing to fabricate the sensing electrodes on a 3-inch glass wafer. The electrodes are 20 μ m in width and the gap between two electrodes is 30 μ m. The electrodes consisted of 100 nm layer of gold on top of a 5 nm adhesive layer of chromium. Microfluidic channel fabrication was divided into two steps: channel mold fabrication and channel fabrication. The channel mold was fabricated using soft lithography. A layer of SU-8 is patterned on a 3-inch silicon wafer involving spin coating, soft bake, exposure, post exposure bake, development, and finally hard bake. The size of channel is 30 μ m in width and 15 μ m in height. The channel pattern was transferred from the mold to a polydimethylsiloxane (PDMS) slab using the following process. Pre-polymer and curing agent were mixed at a ratio of 10:1. Then the mixture was poured onto the channel mold, degassed and baked at 80 °C for 30 minutes to allow for curing.

Afterwards, the mold was peeled off and two holes (one 5 mm and one 1.2 mm) were punched through the PDMS to be used as inlet and outlet. The PDMS slab was covalently bonded onto the glass electrode chip by treating the two substrates with oxygen plasma.

2.4.3 Multi-frequency impedance flow cytometry

Multi-frequency impedance cytometry was performed to measure the electrical impedance responses at 8 different frequencies, ranging from 100 kHz to 20 MHz. To enable capillary driven flow of the test sample, the microfluidic channel was made hydrophilic by treating the chip with oxygen plasma. Fluid flow was actuated by both capillary flow and gravity. The fluid height difference between the inlet and outlet causes a pressure gradient in the channel that drives the fluid. Subsequently, PBS was injected into the channel to preserve the hydrophilicity and improve impedance measurements. To prevent bead aggregation, the sample was ultra-sonicated for 5 minutes immediately before the measurements. PBS was then withdrawn from the channel and beads to be tested were introduced from the inlet. Beads were diluted in 60 μ L PBS to maintain a continuous flow for more than 15 minutes without the use of a syringe pump, which could introduce interference and noise to electrical measurements. The impedance across the electrode pair was modulated by beads passing through due to perturbations of the electric field. The data was captured by a commercial multi-frequency lock-in amplifier (Zurich Instruments HF2A, Zurich, Switzerland). Eight different AC frequency signals generated by the same lock-in amplifier were superimposed to stimulate the electrode. The voltage was set at 0.4 V

to maximize signal power while preventing electrode corrosion. The output voltage is proportional to the impedance between two electrodes. To minimize interference and noise from the environment, the device was placed in a grounded metal box (faraday cage) during measurements.

We tested beads containing different quantities and lengths of DNA. The impedance response data at each concentration/length of DNA were collected from approximately 500 beads. To account for device-to-device variation and perform data normalization, we measured the response of bare streptavidin coated paramagnetic beads in each set of experiments.

Chapter 3: Beadless DNA Assay for DNA sizing

3.1 Introduction

In the previous chapter, we introduced the novel technology for DNA quantification and sizing by measuring the impedance response of the integration of DNA strands and magnetic beads. The use of magnetic beads in the method adds specificity to the measurements and improve the sensitivity by offsetting the impedance. However, it also requires additional purification of beads. The beads can get sticky in the channels which could increase the probability of clogging. Due to the random nature of the number of copies binding to the beads, we need to measure a large number of beads to get an average impedance.

In this work, we analyzed the DNA length based on the bulk impedance of the purified DNA mixture without using the magnetic beads. We investigated the impedance of mixture containing same copies of 209 bp DNA fragments and 538 bp DNA fragments. Blinded experiments were performed to predict the length of DNA in the samples. An accuracy of 88.9% was achieved. The results showed different lengths DNA samples could be identified by their impedance response.

3.2 Methods and Materials

3.2.1 Electrode and microfluidic channel fabrication

Similar to the method written in chapter 2.4, we fabricated the electrodes using standard photolithography, electron beam evaporation, and lift-off process. The electrodes were

patterned by photolithography, followed by deposited 5 nm adhesive chromium layer and 100 nm gold. The geometry of electrodes are 20 μm in width and 30 μm between two electrodes. The microfluidic channel mold was fabricated using lithography. A layer of SU-8 is patterned on a 3-inch silicon wafer involving spin coating, soft bake, exposure, post exposure bake, development, and finally hard bake. The size of channel is 30 μm in width and 15 μm in height. The channel pattern was transferred from the mold to a polydimethylsiloxane (PDMS) slab using the following process. Pre-polymer and curing agent were mixed at a ratio of 10:1. Then the mixture was poured onto the channel mold, degassed and baked at 80 $^{\circ}\text{C}$ for 30 minutes to allow for curing. Afterwards, the mold was peeled off and two holes (one 3 mm and one 1.2 mm) were punched through the PDMS to be used as inlet and outlet. The PDMS slab was covalently bonded onto the glass electrode chip by treating the two substrates with air plasma.

3.2.2 Multi-frequency impedance measurement

Multi-frequency impedance measurement was conducted to capture the electrical impedance responses at 8 different frequencies, ranging from 10 kHz to 10 MHz. The experiment started with making the microfluidic channel hydrophilic using air plasma. DI water was injected into the channel to preserve the hydrophilicity and established the baseline for measurements. After 5 minutes, the DNA sample was introduced to the channel for another 10 minutes measurement. The impedance across the electrodes was tracked by a commercial multi-frequency lock-in amplifier (Zurich Instruments HF2A, Zurich, Switzerland). The output voltage is proportional to the impedance between the

two electrodes. The device was placed in a metal box during measurements to reduce the interference and the noise from the environment.

3.3 Results and discussion

3.3.1 Multi-frequency impedance response of different lengths DNA samples

We measured the impedance of mixtures contained different length (209 bp and 538 bp) but same molar concentration DNA fragments at eight different frequencies. Figure 3-1 shows the impedance spectra of two different length samples. The dotted lines indicate the trend lines by connecting all points. The error bar represents for the standard deviation over five experiments. The 209 bp DNA samples have a larger impedance compared with 538 bp DNA samples below 1 MHz. The nucleotide is negatively charged in the medium. The longer the DNA strand, the more charge it will have, and thus it is more conductive in DI water. As frequency increases above 1 MHz, the difference between the impedance of two samples becomes smaller. The reason for that is the capacitance is getting shorted gradually and hence creates a path to conduct the current. Two samples are more permeable to the electric field, so the impedance decreases and becomes similar to each other. The results indicate that the impedance responses of different length DNA samples are distinct. Our sensor can detect the impedance difference to differentiate different length DNA samples.

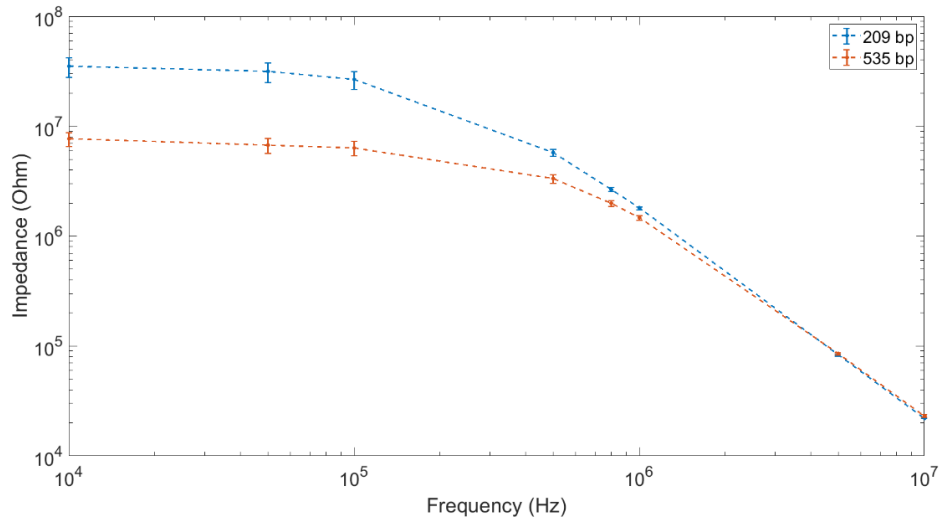


Figure 3-1 Impedance spectra of 209 bp and 358 bp DNA samples.

3.3.2 Prediction of the DNA length based on the impedance

We conducted blinded experiments on DNA samples to validate the use of electrical impedance for DNA sizing. Nine samples were labeled as unknown and measured the impedance at eight frequencies. The length of the DNA in the sample was determined based on the impedance response. The confusion matrix is shown in Figure 3-2. All 538 bp DNA samples were predicted correctly, while one 209 bp DNA sample was predicted wrongly as 538 bp DNA. We achieved an accuracy of 88.9%. It implies that we could use impedance response to predict the length of DNA in the sample.

		True length	
		209 bp	538 bp
Predicted length	209 bp	5	0
	535 bp	1	3

Figure 3-2. Confusion matrix of DNA length prediction

3.3.3 Comparison between bead-DNA assay and beadless DNA assay

Without using beads, this new method reduces sample preparation time. It preserves more PCR products since fewer washing cycles need to be performed. However, the detection limit increases as it is less sensitive compared with the method depicted in the previous chapter.

The quantification score was defined as the summation of output voltage peak amplitude measured at all eight frequencies. In the previous study, the bead attached with longer DNA exhibits a larger quantification score. The results of the beadless DNA assay are shown in impedance in Figure 3-1. The impedance is inversely proportional to the output voltage. The impedance of 538 bp DNA samples is smaller than the impedance of 209 bp DNA samples. Therefore, 538 bp DNA samples have a larger output voltage amplitude than 209 bp DNA samples, which is consistent with what we observed in the previous study. Figure 3-3 shows the quantification score of 209 bp and 538 bp DNA samples, where the 538 bp DNA samples have a larger

quantification score than 209 bp DNA samples. The results of the two studies are consistent with each other.

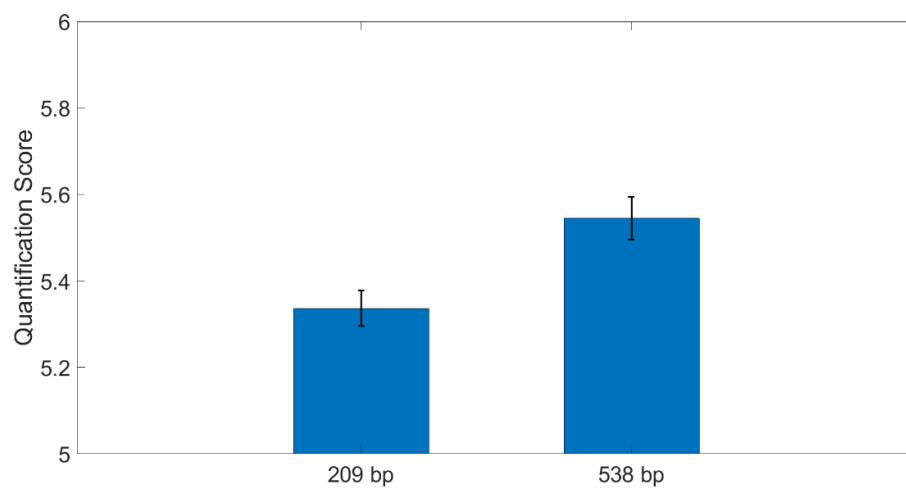


Figure 3-3. Quantification score of 209 bp and 538 bp DNA samples.

Chapter 4: Electronic classification of barcoded particles for multiplexed detection using supervised machine learning analysis

4.1. Introduction

In this work, we develop a new fabrication method for the barcoded particles along with novel data analytics to expand the barcode library to nine particles. We expand the library of barcoded particles using varying oxide thicknesses and dielectric properties. We also report a new finding that a single thin-film dielectric layer is sufficient for particle barcoding, eliminating the need for an intermediate gold layer, thus simplifying fabrication. We perform a basic study of the fabrication parameters involved in the barcoded particles, and assess the classification accuracy.

Recently, many interests have developed in utilizing machine learning techniques to enhance both sensitivity and classification of biosensors [106-108]. Without being explicitly programmed, machine-learning algorithms could help classify different biomolecules. Supervised machine learning allows for training a classifier with labeled data described by many features, whereby the classifier determines the optimal boundary for accurately classifying the data. The accuracy of the classifier is then assessed using test data with known values. The support vector machine (SVM) is a broadly used supervised machine learning algorithm technique for classification and regression analysis [109, 110]. In this work, we perform measurements of barcoded particles using multi-frequency impedance cytometry and utilize the amplitude of the barcoded particles at each frequency as features for the SVM classifier to enhance our ability to accurately classify particle barcodes.

4.2. Methods and Materials

4.2.1 Barcoded particle fabrication

The fabrication process of barcoded particles is showed in Figure 4-1. It starts with forming a single layer of 3 μm polystyrene beads on a glass substrate using dip-coating. As the liquid evaporates, the bead gradually assembles together under inter-particle forces. After wiping out the polystyrene beads accumulated on the back side, atomic layer deposition (ALD) was performed to deposit a layer of oxide on top of remained polystyrene beads. To avoid melting of the polystyrene particles, the operation temperature of ALD was set to 150 $^{\circ}\text{C}$. In this work, we deposit different oxides (alumina, hafnia and titania) of different thicknesses (10 nm, 20nm and 30 nm) on bare polystyrene beads to form different barcoded particles. At last, barcoded particles are collected in phosphate buffered saline (PBS) with ultrasonication for agitation.

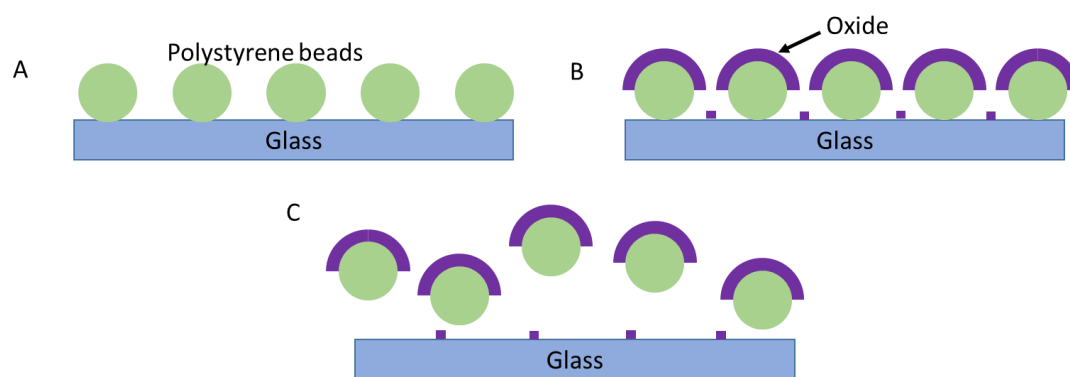


Figure 4-1. Fabrication process of barcoded particles. A) Formation of self-assembled monolayer on glass by dip-coating glass slide. B) Deposition of oxide layer using atomic layer deposition (ALD). C) Re-suspension of particles to solution using ultrasonication.

4.2.2 Sensor design and fabrication

The sensor is designed to measure the electrical impedance of barcoded particles at multi-frequency. It consists of two parts, sensing electrodes and microfluidic channel, as shown in Figure 4-2A and 4-2B. Two coplanar electrodes are designed as 20 μm in width and the gap between two electrodes is 30 μm . To improve the sensitivity while minimize clogging, the microfluidic channel size is set as 15 μm in height and 30 μm in width. Sensing electrodes are fabricated through standard photolithography process on 3 inch glass wafer. The first step is patterning photoresist, which includes cleaning wafer, spin coating photo resist, pre-bake, aligning mask and wafer, exposing UV light, developing and post-bake. Then, 5 nm chromium and 100 nm gold are deposited sequentially on the wafer using electron beam evaporation. At last, unintended metal is removed by lift off process.

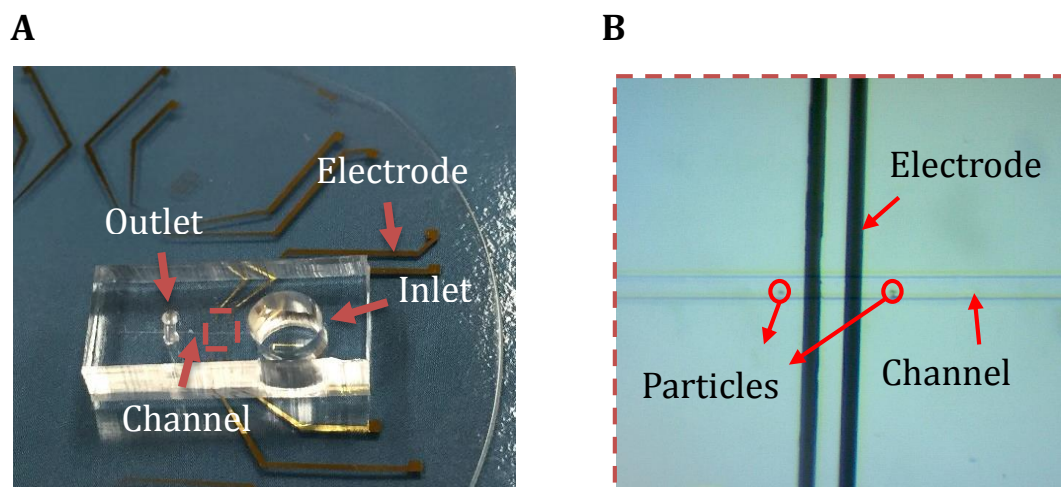


Figure 4-2. A) Schematic diagram of a multi-frequency impedance flow cytometer for classifying nanoelectronic barcoded particles. B) Image of the device.

Microfluidic channel is fabricated using soft lithography technique. The channel molding is made by patterning a layer of SU-8 on a 3-inch silicon wafer using the similar process as described above. Then, transfer the channel pattern from channel molding to a polydimethylsiloxane (PDMS) slab. The process contains mixing pre-polymer and curing agent at ratio of 10:1 sufficiently, pouring the mixture onto the channel mold, degassing for 15 minutes to remove bubbles and baking at 80 °C around 30 minutes for curing. Afterwards, 5 mm inlet well and 1.2 mm outlet well are punched. At last, the microfluidic channel is bonded onto the electrode patterned glass wafer by implementing plasma treatment.

4.2.3 Frequency-dependent impedance modulation

By depositing oxides of different materials and thicknesses on particles, the overall frequency-dependent impedance of the particle is tuned. Previous work [65] has shown that an insulative layer can modulate the Claussius-Mossotti (CM) factor, which describes the frequency dependence of the effective polarization, given by Eq. (1).

$$f_{CM}(\omega) = \frac{\tilde{\epsilon}_p - \tilde{\epsilon}_m}{\tilde{\epsilon}_p + 2 \cdot \tilde{\epsilon}_m} \quad (1)$$

where

$$\tilde{\epsilon}_m = \epsilon_m - \sigma_m / j\omega \quad (2)$$

The CM factor is determined by the complex permittivity of the barcoded particle ($\tilde{\epsilon}_p$) and the buffer medium ($\tilde{\epsilon}_m$). The complex permittivity consists of both the dielectric constant (ϵ) and conductivity (σ). The barcoded particle is asymmetric and the CM

factor can be calculated as the average of CM factors of a sphere and a layered particle [111]. The complex permittivity of a layered particle is given by the following equation [112]:

$$\tilde{\epsilon}_{eff} = \tilde{\epsilon}_{out} \cdot \frac{\left(\frac{R_{out}}{R_{in}}\right)^3 + 2\frac{\tilde{\epsilon}_{in} - \tilde{\epsilon}_{out}}{\tilde{\epsilon}_{in} + 2\tilde{\epsilon}_{out}}}{\left(\frac{R_{out}}{R_{in}}\right)^3 - 2\frac{\tilde{\epsilon}_{in} - \tilde{\epsilon}_{out}}{\tilde{\epsilon}_{in} + 2\tilde{\epsilon}_{out}}} \quad (3)$$

where $\tilde{\epsilon}_{eff}$ is the effective complex permittivity of entire particle, $\tilde{\epsilon}_{out}$, $\tilde{\epsilon}_{in}$ are the complex permittivity of the outer layer and the inner core respectively. R_{out} is defined as the radius of the entire particle (including the inner core) and R_{in} designates the radius of inner core. Previous studies demonstrated that the CM factor is directly related to the impedance [113]. Hence, impedance will also be effected as the CM factor is tuned. This could be expressed by Eq. (4),

$$Z(\omega) = \frac{\kappa}{j\omega\tilde{\epsilon}_m} \cdot (1 - 3 \cdot \phi \cdot f_{CM}) \quad (4)$$

where κ is a geometric constant, given by the ratio of electrode area to electrode separation and ϕ is the volume fraction occupied by the particle.

4.2.4 Multi-frequency impedance cytometry

Differing thicknesses of the oxide layer and different oxide materials modulates the particle surface conductance, permittivity, and charging profile, thus tuning the Claussius-Mossotti factor and modulating the frequency dependent impedance. Using a micro-impedance cytometer (sensor), which contains micro-electrodes integrated with a micro-channel, in conjunction with a multi-frequency lock-in amplifier (Zurich Instruments HF2A, Zurich, Switzerland), we capture the impedance response of

barcoded particles at multiple frequencies. The schematic diagram is shown in Figure 4-3. We obtain impedance data at 4 frequencies simultaneously in one measurement and implemented 4 different measurements for each type of barcoded particles (16 frequencies in total ranging from 100 kHz to 30 MHz). We limited the measurement to 4 frequencies to prevent electrodes from burning out, as more current is pumped into the electrodes per each extra frequency added to the measurement. In each frequency measurement, 500 kHz was used as a standard frequency for control. The electrodes get stimulated by a combination of 4 different frequency AC signals provided by the lock-in amplifier.

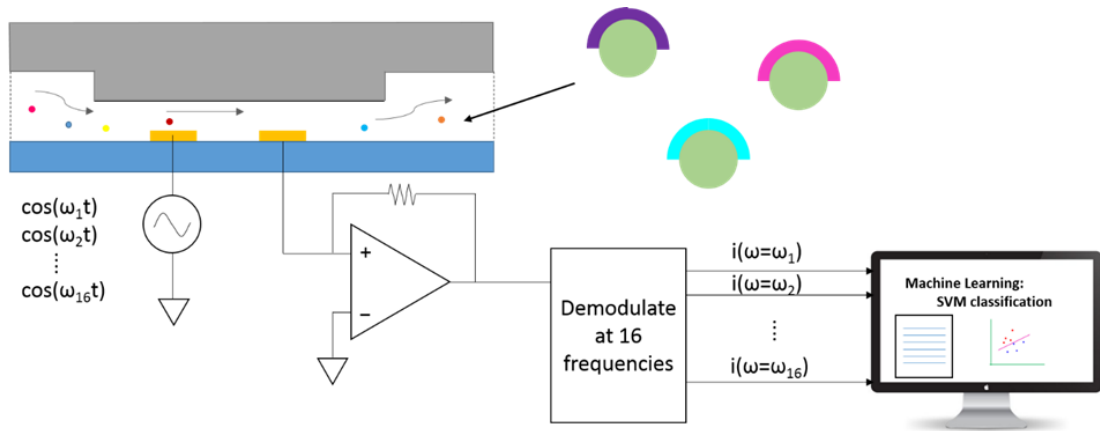


Figure 4-3. Schematic diagram of a multi-frequency impedance flow cytometer for classifying nanoelectronic barcoded particles.

The experiments starts by making the microfluidic channel hydrophilic using oxygen plasma treatment. We fill the channel with PBS to preserve the hydrophilicity until the measurement begins. Particles are introduced to the channel from inlet well after removing the PBS. Under the gravity and the pressure gradient in the channel, which is caused by the inlet and outlet fluid height difference, particles continuously flow

through the channel [114]. When the particle passes the sensing region, it interferes the ions conducting between electrodes and thus changes the impedance across the electrodes. This change is captured by the lock-in amplifier and the signal is demodulated at the same frequency used for stimulation. To screen the noise and interference from the environment, the device was placed in a metal box during the experiment.

4.2.5 Machine learning analysis

To enable better classification of different barcoded particles, we employed a commonly used supervised machine learning classifier, the support vector machine (SVM). For each particle barcode, we performed the multi-frequency impedance measurements. The peak intensity at each frequency is used as a feature. We train the SVM model with half of the data and test with the other half data. A 5-fold cross validation is implemented to protect against overfitting. A Gaussian kernel is chosen for SVM training and testing. By comparing the predicted category and the true class, we are able to determine the accuracy of the SVM classifier, which, in turn, also depicts the impedance difference between different barcoded particles. The analysis is implemented in Matlab (Mathworks, MA, USA) using Classification Learner toolbox.

4.3. Results

We expand the barcoded particle library using atomic layer depositing oxides of varying thickness and dielectric permittivity. Nine different particles are involved in

the barcode library, including bare polystyrene beads, polystyrene beads coated with 10 nm, 20 nm and 30 nm alumina, polystyrene beads coated with 10 nm, 20 nm and 30 nm hafnia and polystyrene beads coated with 10 nm and 20 nm titania.

4.3.1 Impedance response of particles at multiple frequencies

Figure 4-4 shows representative multi-frequency (7.5 MHz, 10 MHz and 15 MHz) time series data of bare polystyrene beads and polystyrene beads coated with 20 nm alumina in a time window of 5 seconds. The lock-in amplifier measures the current flowing out of the electrode. Then converts the current to the voltage and demodulates at the desired frequency. Thus, the voltage is proportional to the impedance across two electrodes. The voltage is normalized to the baseline in the time window for ease of comparison. As shown in the figure, the voltage peak intensity decreases as frequency increases. This can be attributed to the surface capacitance of the beads, which gets shorted gradually as frequency increases and hence decreases the overall impedance. The barcoded particles have smaller impedance peak intensity at higher frequencies compared with bare polystyrene beads because of the larger surface capacitance [65, 115]. As the data indicates, analyzing impedance at multiple frequencies can allow differentiation of barcoded particles from each other.

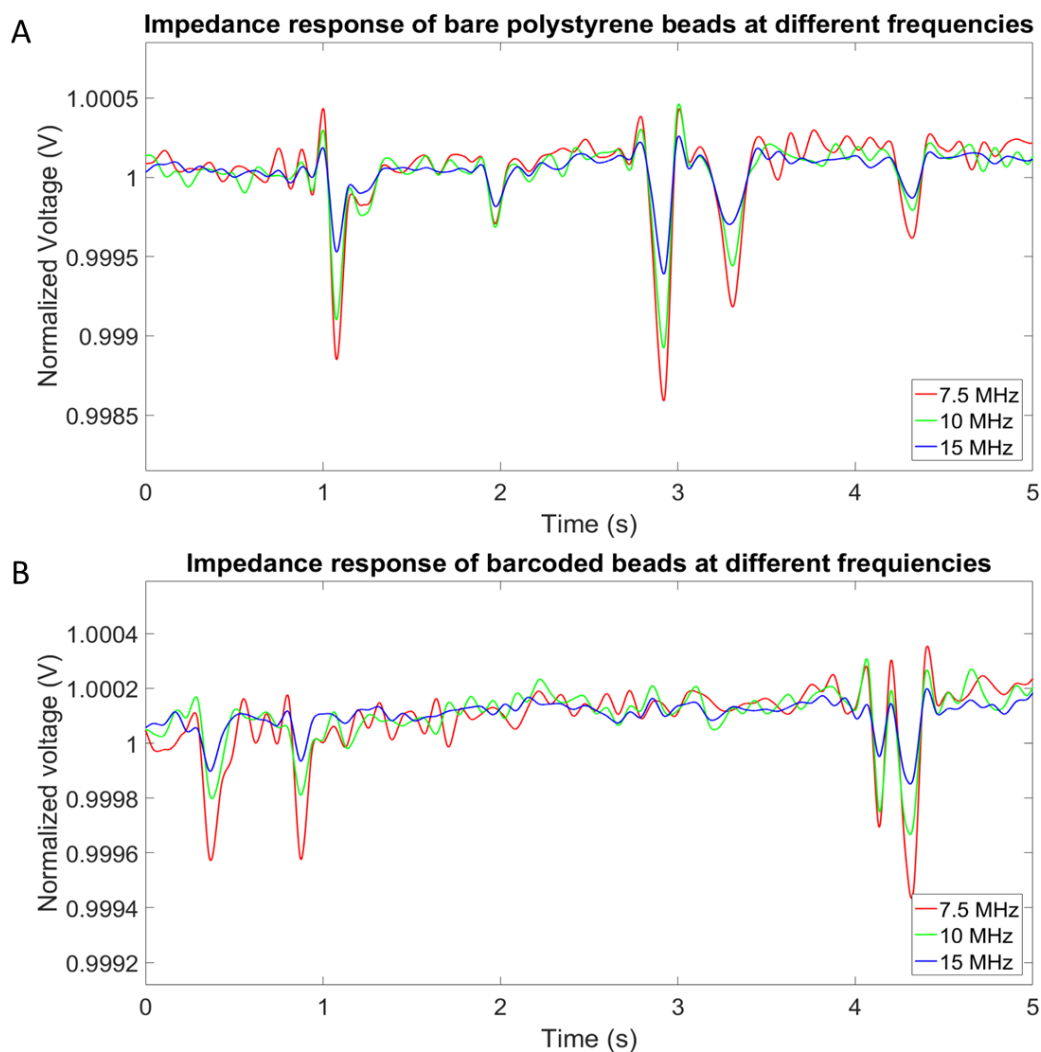


Figure 4-4. Representative data of different beads passing through the sensing region measured at 7.5 MHz, 10 MHz, and 15 MHz respectively. A) Bare polystyrene beads B) Barcoded beads.

4.3.2 Effect of oxide layer thickness

We studied impedance modulation effects of oxide layers of different thicknesses for a given oxide. In the case of particles with a deposited alumina or hafnia layer, we studied 10 nm, 20 nm, and 30 nm thick layers. In the case of titania, we studied 10 nm and 20 nm layers. Figure 4-5 shows the impedance response of different materials with

different thickness. The peak amplitude refers to the intensity of impedance change resulting from a particle passing through the sensing region of the channel. Different frequencies were chosen to show the best separation of different barcoded particles. Figure 4-5A shows the scatter plot of peak intensities of alumina barcoded particles of 3 different thicknesses at two different frequencies ($f = 500$ kHz and $f = 15$ MHz). 20 nm alumina barcoded particles exhibit the largest voltage peak on average at 500 kHz, while 10 nm alumina barcoded particles demonstrate the largest voltage peak on average at 15 MHz. In Figure 4-5B, the impedance responses of different thicknesses of hafnia at $f = 500$ kHz and $f = 5$ MHz are depicted. The impedance responses of 20 nm and 30 nm hafnia barcoded particles overlap with each other, yet they are both distinguishable from the impedance of 10 nm hafnia barcoded particles. The thickness of titania has a larger difference on impedance response, as shown in Figure 4-5C. The peak amplitude of particles coated with 20 nm titania is on average larger than that of particles coated with 10 nm titania at both $f = 500$ kHz and $f = 2$ MHz. This is because the dielectric constant of titania is much larger than the other oxides, and thus result in larger impedance change for the same increase in oxide thickness compared with hafnia or alumina.

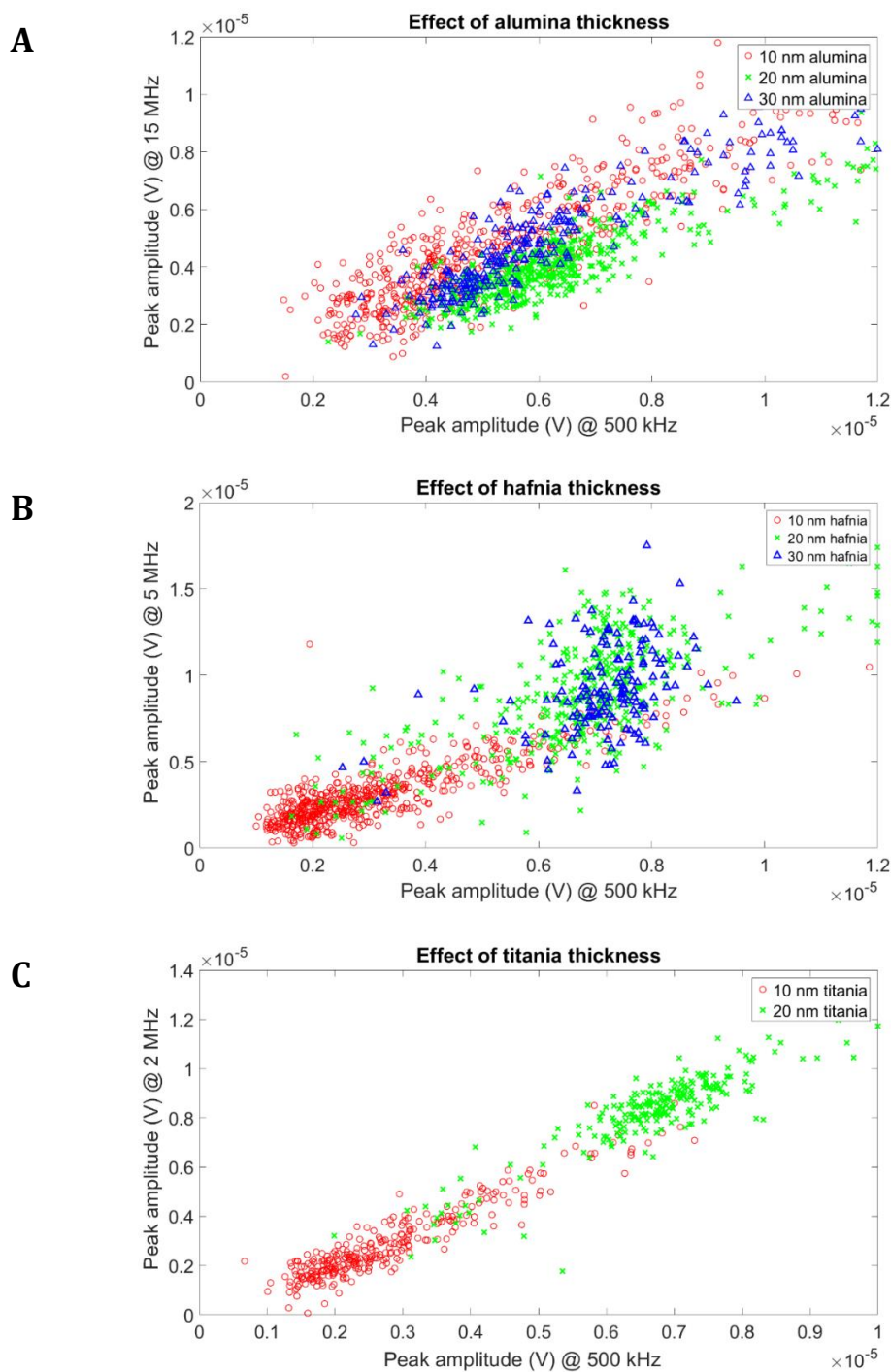


Figure 4-5. The impedance responses of barcoded particles with different thickness oxides. A) Scatter plot of peak amplitude @ 500 kHz vs. peak amplitude @ 15 MHz of particles with different alumina thickness. B) Scatter plot of peak amplitude @ 500 kHz vs. peak amplitude @ 5 MHz of particles with different hafnia thickness. C) Scatter plot of peak amplitude @ 500 kHz vs. peak amplitude @ 2 MHz of particles with different titania thickness.

Machine learning analysis is implemented to enhance the classification ability. The bar graphs in Figure 4-6 and Figure 4-7 demonstrate the accuracy of SVM model in differentiating between barcoded particles with the same dielectric, yet different oxide thicknesses. The accuracy in discriminating between particles coated with 10 nm titania from 20 nm titania is 96%. Overall, the SVM classifier could distinguish alumina and hafnia barcoded particles from each other with high accuracy, with the exception of particles deposited with 20 nm and 30 nm hafnia, whose impedance responses also significantly overlap with each other in the scatter plot. Based on this information, it implies that when developing a multiplexed assay, it is important to properly select only the barcodes that can be classified with high levels of accuracy.

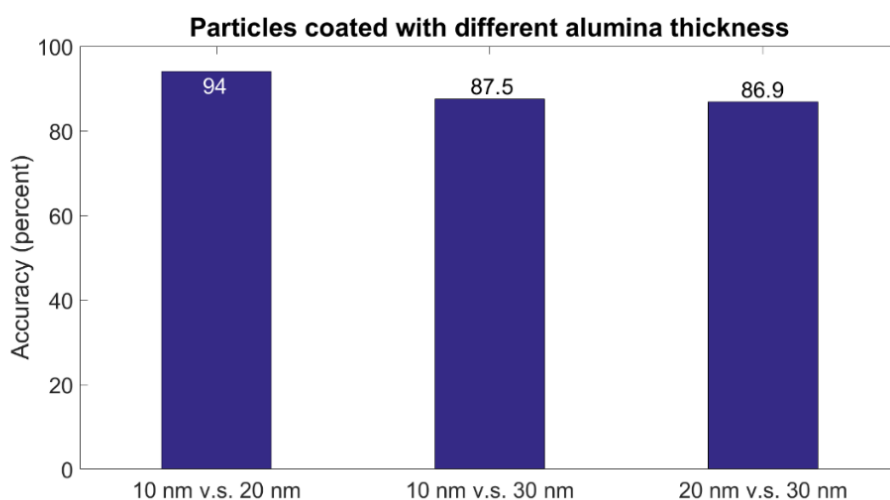


Figure 4-6. The accuracy of SVM model differentiating particles with different thickness of alumina.

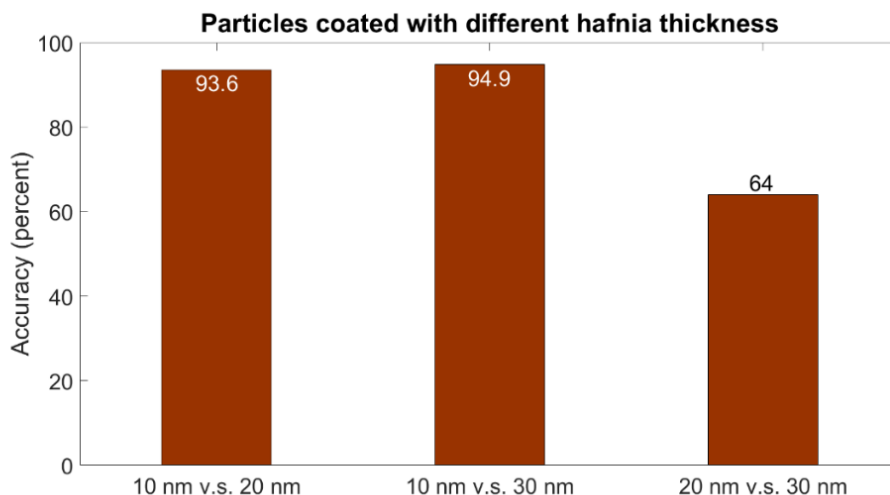


Figure 4-7. The accuracy of the SVM model differentiating particles with different thickness of hafnia.

4.3.3 Distinction between particles coated with different dielectric layers

Besides oxide layer thickness, we also studied the effect of oxide permittivity. We compared the impedance response of particles coated with insulators of the same thickness but different dielectric materials. The scatter plot of peak intensity at two different frequencies is shown in Figure 4-8. Different frequencies were chosen to show the best separation of different barcoded particles. In Figure 4-8A, the response of particles deposited with 10 nm of different insulators is depicted. The particles coated with alumina has the largest voltage peak amplitude at both 500 kHz and 20 MHz, while particles coated with hafnia or titania, experience smaller current drop when barcoded particle passing through the sensing region. In Figure 4-8B, particles coated with 20 nm hafnia or titania show a response similar to the 10 nm situation. However, the peak intensity of particles coated with alumina is smaller than hafnia and titania at

both 500 kHz and 5 MHz. In Figure 4-8C, the particles coated with the 30 nm oxide layer can be easily distinguished from each other at both 500 kHz and 15 MHz.

We performed SVM analysis to quantify the discrimination between barcoded particles with different dielectric layers. The accuracy in discriminating between particles coated with 30 nm alumina from 30 nm hafnia is 91%. As shown in Figure 4-9A and Figure 4-9B, the SVM result also indicates that the difference between hafnia and titania is smaller than others, which is consistent with the response seen in the scatter plots. From the results, barcoded particles with a 20 nm oxide layer can be more easily distinguished from that of a 10 nm oxide layer, which suggests we should use particles with thicker oxide layers in multiplexed analysis for better discrimination.

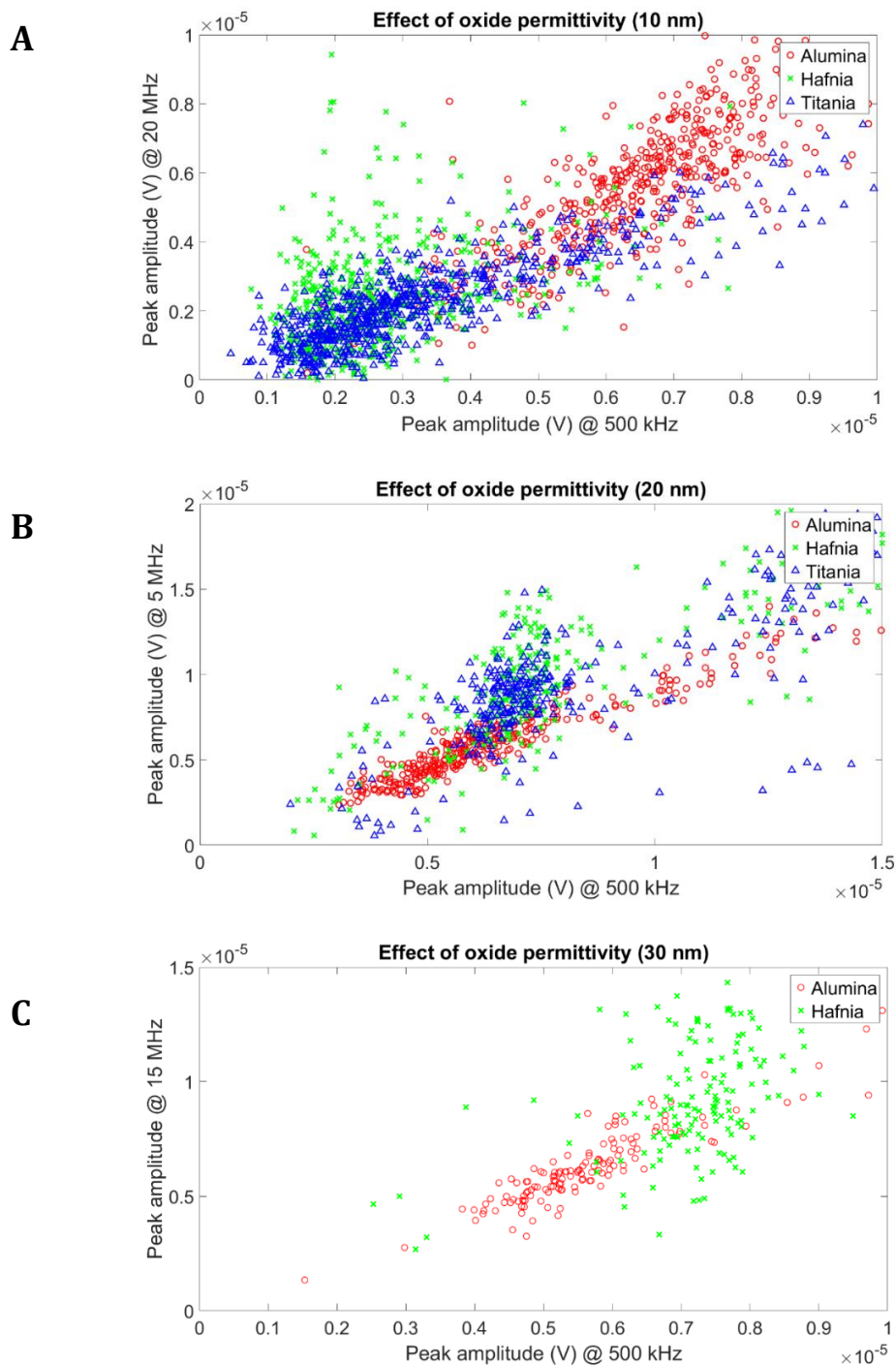


Figure 4-8. The impedance responses of barcoded particles with different dielectric oxides. A) Scatter plot of peak amplitude @ 500 kHz vs. peak amplitude @ 20 MHz for particles with 10 nm different oxides. B) Scatter plot of peak amplitude @ 500 kHz vs. peak amplitude @ 5 MHz for particles with 20 nm different oxides. C) Scatter plot of peak amplitude @ 500 kHz vs. peak amplitude @ 15 MHz for particles with 30 nm different oxides.

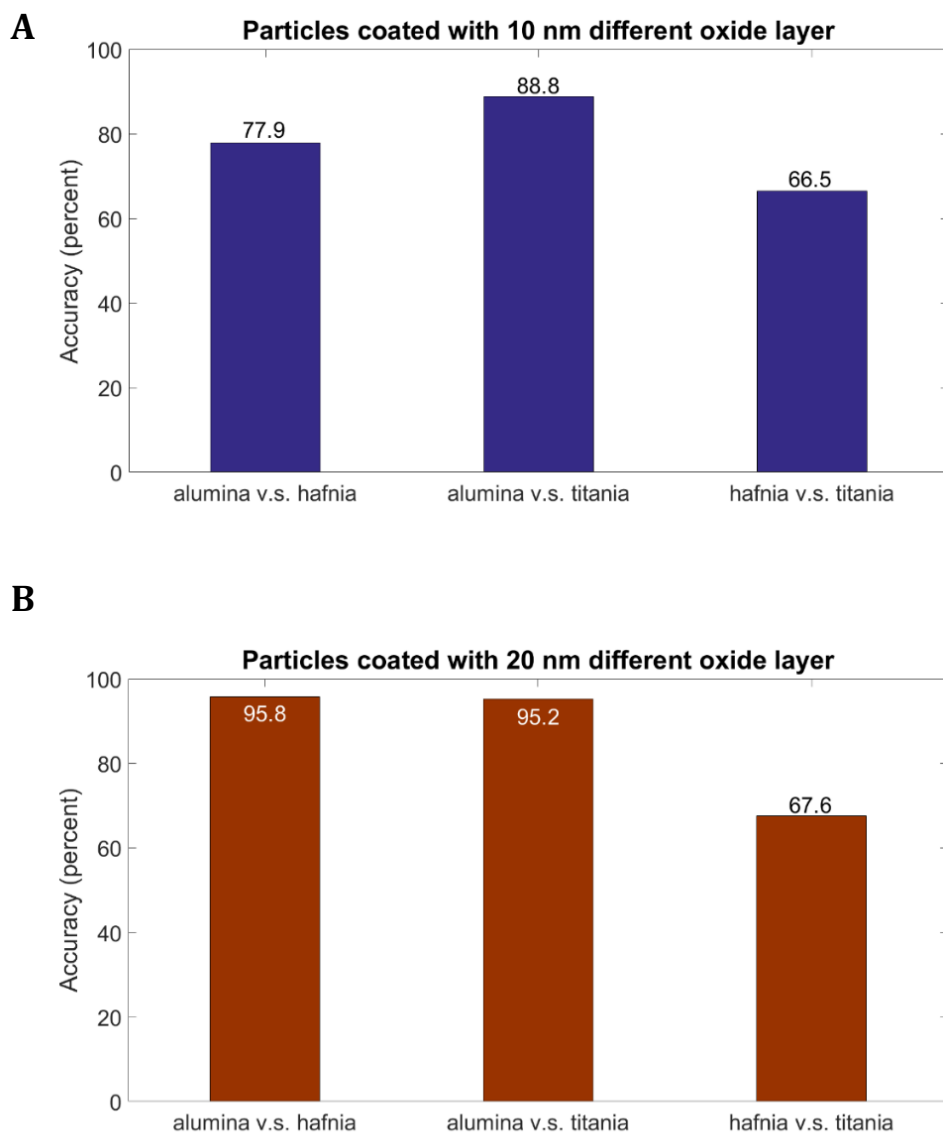


Figure 4-9. SVM results on differentiating barcoded particles with different dielectric oxides. A) The accuracy of SVM model differentiating particles with 10 nm different oxides. B) The accuracy of SVM model differentiating particles with 20 nm different oxides.

4.4. Discussion

The results presented in this paper demonstrate the ability to tune the impedance spectrum of particles by depositing insulation layers of varying thickness and dielectric

materials. Supervised machine learning in conjunction with multi-frequency impedance cytometry can be used for readout and classification of the particles. The additional novelty of this work is that we demonstrated that a single thin-film dielectric layer is sufficient for particle barcoding, and one can omit the use of an intermediate gold layer, thus simplifying the fabrication process. We fabricated 9 single dielectric layer barcoded particles using this simplified process. By implementing SVM machine learning algorithm, we enhanced the classification ability to distinguish barcoded particles. As a result, these particles can be selected and utilized as barcodes in a functional biomarker assay to improve the throughput in the future.

For future work involving a multiplexed assay, our results provide guidance for selection of particles: 1) 20 nm hafnia and 30 nm hafnia particles should not be used together in the same assay. 2) Similar thickness of hafnia and titania particles should be avoided in the same assay mixture. 3) When using insulators of the same thickness but different permittivity in a single assay, 20 nm particles can provide better discrimination compared with 10 nm.

Another notable result is that the change in impedance does not necessarily change linearly with oxide thickness change. The underlying reason behind this requires further study. For particles coated with 20 nm hafnia and 30 nm hafnia, the impedance responses are similar. One possibility is that there is a threshold thickness for each dielectric, beyond which the impedance will not further change. Future efforts will be dedicated to gaining a more clear understanding of these questions and applying the particles to performing multiplex protein biomarker assays. This manuscript is focused electronically discriminating between the different barcodes. Potential methods for

quantification of the biomarkers using these barcodes has previously been discussed elsewhere [32, 65, 116].

4.5. Conclusion

In this paper, the barcode library is expanded to nine barcoded particles by depositing different thicknesses and types of oxide layers on top of bare polystyrene beads. We demonstrate the single layer of oxide could sufficiently modulate the frequency dependent impedance and thus eliminate the need for the intermediate gold layer and simplify fabrication. A micro-impedance cytometer (sensor) is designed and fabricated to perform multi-frequency impedance cytometry, where the PDMS-based microfluidic channel is covalently bonded onto the surface of electrode glass chip. By implementing impedance measurements at multiple frequencies in conjunction with machine learning analysis, we demonstrate the capability of our sensor to detect different particle barcodes. Finally, we provide systematic guidelines for selection of particle barcodes to be used in a multiplexed biomarker assay in the future.

Chapter 5: Electrical impedance as an indicator of microalgal cell health

5.1. Introduction

In this project, we present a novel method to study algal cell phenotype using electrical impedance cytometry at multiple frequencies, providing an instantaneous snapshot of organism dielectric properties at the single cell level. We investigated the frequency-dependent impedance of bacterium-size (i.e., 2-3 μm cell diameter) green algal cells (*Picochlorum* SE3, Chlorophyta) [117, 118]. The algae were cultured in three different salinity conditions and sampled at four different time points over a wide frequency range using a multi-frequency lock-in amplifier that was utilized in conjunction with a microfluidic channel. We demonstrate the utility of electrical impedance as a phenotype indicator that reflects the change in size and permeability of cells under different salt stresses.

5.2. Results

5.2.1 Microfluidic sensor design and electrical impedance analysis

We built a microfluidic sensor to perform multi-frequency impedance cytometry to capture the impedance information of algal cells. As shown in Figure 5-1, the instrument comprises two components, two pairs of coplanar golden electrodes deposited on a glass substrate and a polydimethylsiloxane (PDMS) microfluidic channel. To enhance sensitivity and prevent blockage, the channel dimension was 30

μm in width and $8\ \mu\text{m}$ in height. The width of the two electrodes was $20\ \mu\text{m}$ and the gap between them was $20\ \mu\text{m}$. In the experiments we describe below, only one pair of electrodes was used for measurement. When a cell flows through the sensing region, it occludes a portion of the ionic current conducting between the two electrodes. Thus, the current decreases, and conversely the impedance increases. The closer the dimensions of the sensing region to the size of algal cells, the more current is obstructed and the larger the impedance change. However, blockage is more likely to happen when the channel size is reduced. A commercial multi-frequency lock-in amplifier (Zurich Instruments HF2A, Zurich, Switzerland) was used to capture the impedance change simultaneously at eight different frequencies (ranging from $500\ \text{kHz}$ to $30\ \text{MHz}$).

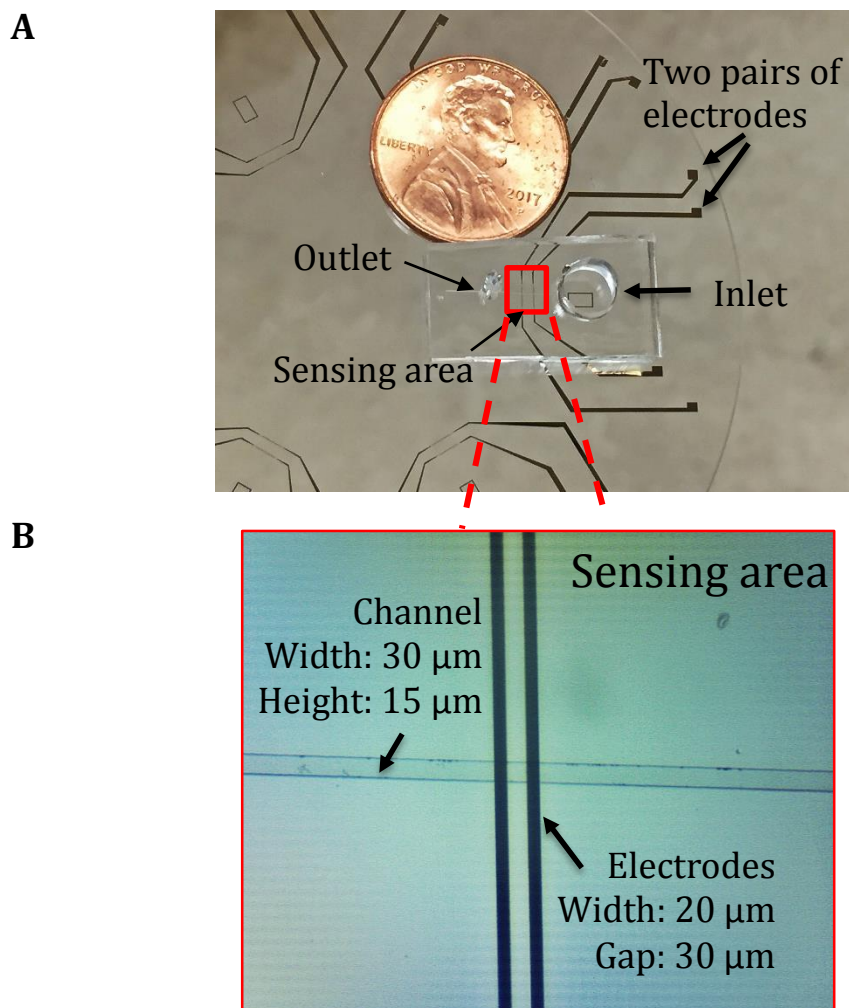


Figure 5-1. Microfluidic sensor. A) Image of the device whereby a soft-lithography made PDMS microfluidic channel is bound onto a glass wafer patterned with two pairs of sensing electrodes. B) Microscope image of the channel and electrodes.

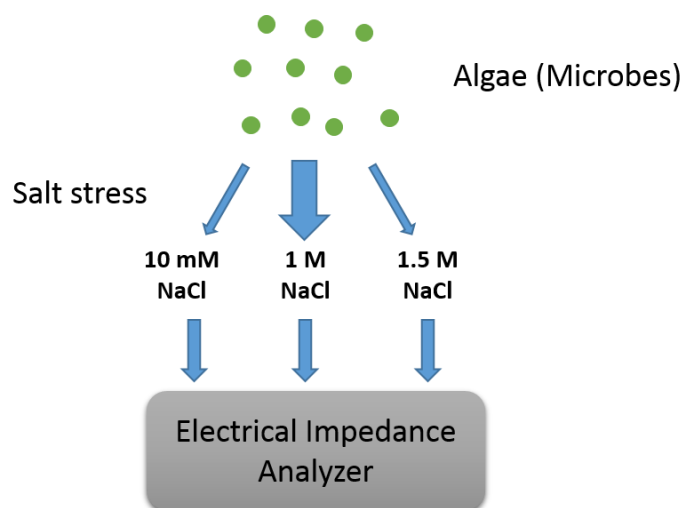
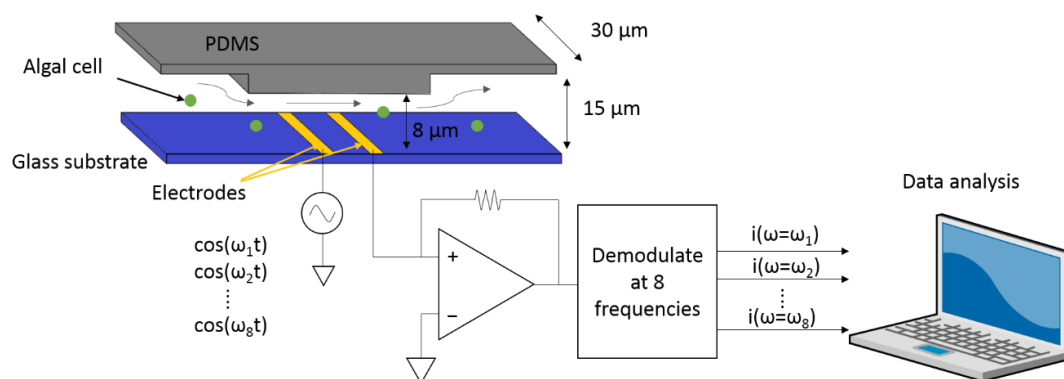
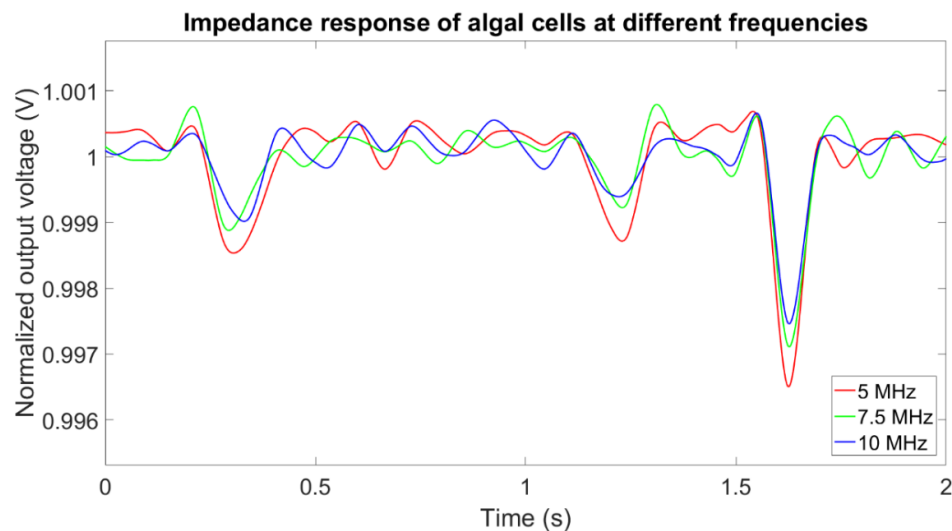
A**B**

Figure 5-2. Overview of strategy. A) Diagram showing the experimental design of the cell impedance experiments in which *Picochlorum* SE3 cells were cultured under widely different salinity conditions (10mM, 1.5M NaCl) after being acclimated to 1M NaCl, and sampled at 4 different time points (1 h, 5h, 1d, and 5d). After culturing, all cells were washed three times in PBS buffer and injected into the electrical impedance analyzer to collect the data. B) Schematic diagram of the electrical impedance measurement. Algal cells were introduced into the channel from the inlet well. When cells flowed through the sensing region, they blocked part of the ions conducting current between the two electrodes. As a result, the impedance changed in this region. This change was captured by a lock-in amplifier at eight different frequencies. The data were transferred to the attached computer for downstream analysis.

Output voltage is proportional to impedance between the two electrodes (sensing region). As described above, when a cell flows through the sensing region, the current between two electrodes decreases, thus the output voltage of the lock-in amplifier decreases and a negative peak is observed. The larger the output voltage peak amplitude, the greater the cell impedance. The peak amplitude is calculated as the difference between the output voltage baseline and the minimum value of the peak. The typical impedance change (output voltage) at different frequencies (5 MHz, 7.5 MHz and 10 MHz) when a cell passes by in a 2-second time window is shown in Figure 5-3A. Traces were normalized using the baseline to allow between-frequency comparison. Previous work from Sun et al. [81] and Gawad et al. [83] demonstrated that a cell can be modeled as a membrane resistance, in parallel with membrane capacitance, and then in series with the cytoplasm resistance, in parallel with cytoplasm capacitance (Figure 5-3B). The C_{dl} and C'_{dl} are the double layer capacitance that surrounds the electrodes and algal cells, respectively, and they will have less impact on impedance when the frequency exceeds several kilohertz. As the frequency increases above 5 MHz, the membrane capacitance gradually gets shorted and thereby creates a path for conducting the current. As a result, the cell becomes more permeable to the electric field generated by the electrodes, and has lower impedance. As the frequency increases, cell impedance depends more on properties of the cytoplasm. In contrast, under a low frequency range (<500 kHz), cell size dominates the impedance [83]. To minimize the effect of variation in cell size on impedance, we defined cell transparency as the ratio of voltage peak intensity (voltage peak amplitude) at higher frequency over peak intensity at 500 kHz, whereby the peak intensity corresponds to size. The cell

transparency reflects cell properties independent of size and also denotes the extent of similarity between the cell and the background solution in the electric field.

A



B

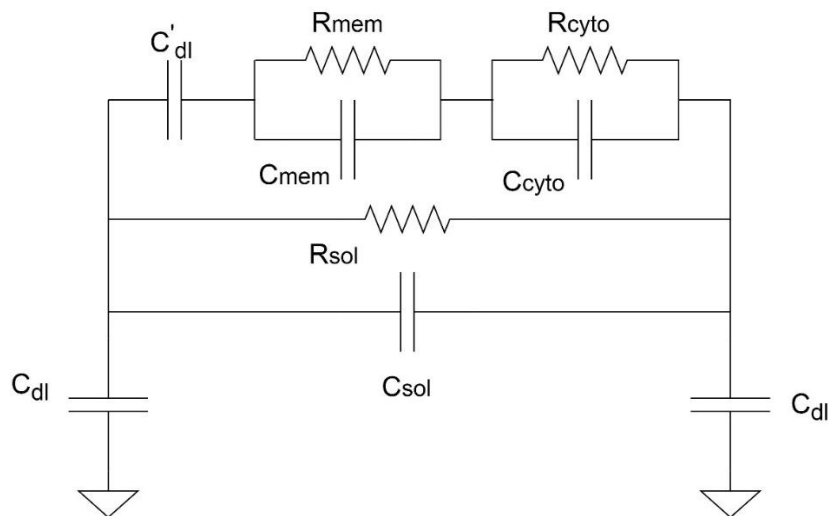


Figure 5-3. Impedance response analysis. a) Representative data for algal cells flowing through the sensing electrodes, measured at 5 MHz, 7.5 MHz and 10 MHz. The line colors denote the different frequencies used (see legend) and the three peaks denote three cells flowing through the sensing area in this 2-second window. b) Impedance model of the cytometer system with the algal cell present. C'_{dl} is the double layer capacitance of the cell. The impedance of cell is in parallel with the solution resistance and capacitance. C_{dl} is the double layer capacitance of the electrodes.

5.2.2 Impedance analysis of algal cell viability

Initially, we studied the impedance responses of live and dead *Picochlorum* SE3 cells. The algae were killed by treating them with heat for 1 h. Multi-frequency impedance flow cytometry was performed to measure the impedance of cells. Both live and dead cells were diluted in 50 μ L of 1X phosphate buffered saline (PBS) immediately before the measurement to allow higher sensitivity. The results of these analyses are shown in Figure 5-4. As apparent in Figure 5-4A, the mean cell transparency of live cells was greater than that of dead cells. The transparency was calculated using average peak intensity measured at 20 MHz over average peak intensity measured at 500 kHz. The peak intensity at 20 MHz reflected more the cytoplasmic permeability, whereas the peak intensity at 500 kHz was affected primarily by cell diameter [83]. These results indicate that dead cells are more transparent to the surrounding electric field, because ions in the media can flow more freely through the membrane. The impedance scatter plot of live and dead cells is shown in Figure 5-4B. Dead cells exhibit smaller peak intensity at 500 kHz, implying that they are smaller in size compared to live cells. The cytoplasmic permeability of dead cells was greater than that of live cells, as can be concluded from the smaller peak intensity of dead cells at 20 MHz. In addition, dead cells have a narrower distribution compared with live cells. In other words, dead cells exhibit more homogeneity in terms of size and permeability. With regard to the frequency response of live and dead cells (Figure 5-4C), the peak intensity difference was small at 500 kHz but became larger as the frequency increased to 25 MHz. This difference became small again at 30 MHz. This pattern illustrates that the size

difference between live and dead cells is smaller compared to the difference in cytoplasmic permeability, as depicted in Figure 5-4B.

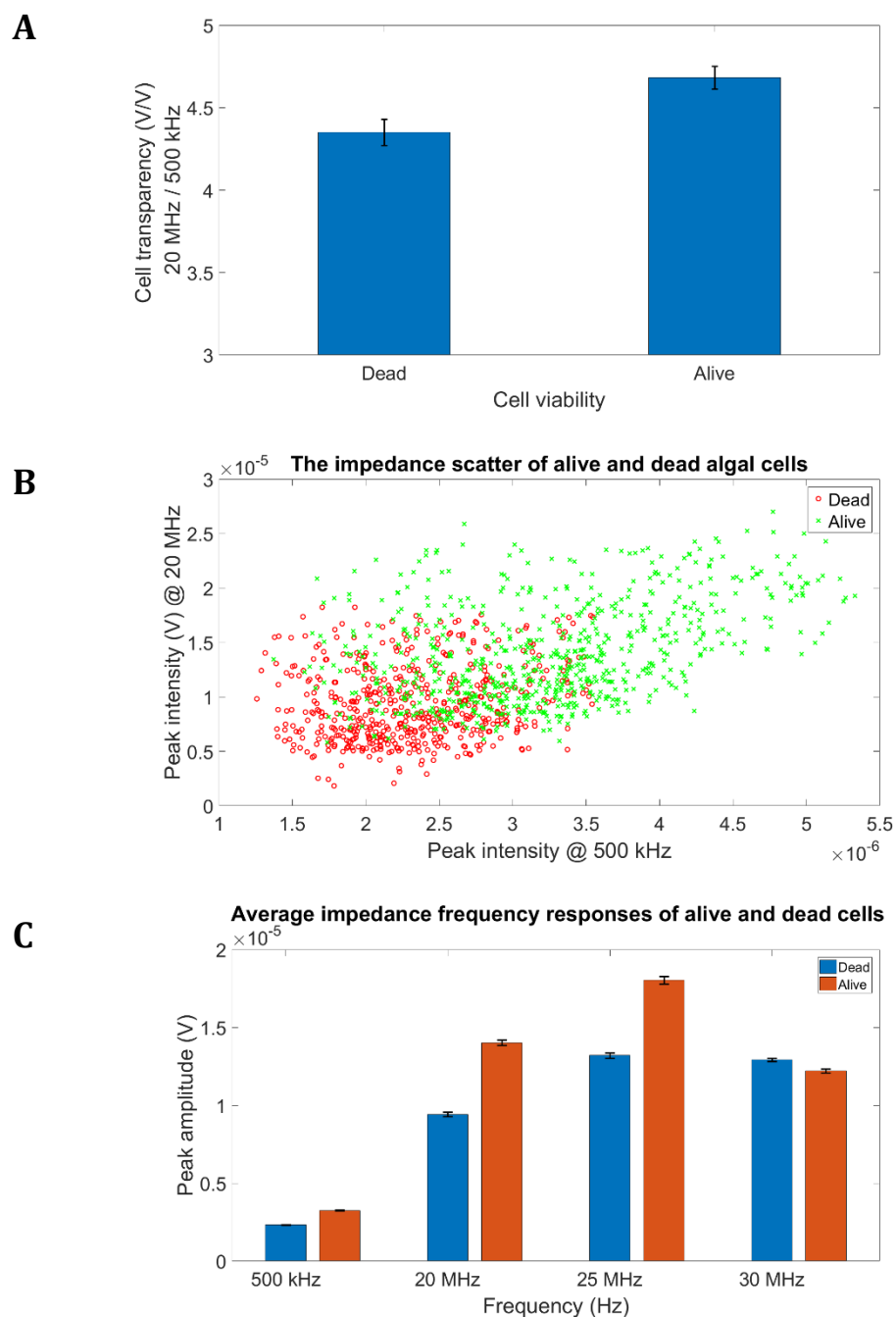


Figure 5-4. Impedance response of live and dead algal cells. A) Average cell transparency calculated using peak intensity measured at 20 MHz over peak intensity measured at 500 kHz. B) The impedance scatter of live and dead algal cells. C) Average impedance frequency response of live and dead algal cells.

These results demonstrate the utility of electrical phenotype for studying not only the viability of algal cells, but also the health of a population.

5.2.3 Algal cell stress analysis using impedance flow cytometry

Algal cells stressed at different salinities. We measured the impedance responses of *Picochlorum* SE3 cells cultured in media of different salinities (0 M, 0.1 M 0.3 M, 0.7 M, and 1.3 M NaCl) for 1 h using multi-frequency impedance flow cytometry. For this approach, 3 mL of algal cells were centrifuged, washed three times with 1X PBS and diluted in 50 μ L PBS. For the control, we measured the impedance response of polystyrene (PS) beads that were incubated in PBS amended with different amounts of salt (0 M, 0.1 M 0.3 M, and 0.7 M NaCl) for one hour. The beads were handled in the same way as the algal cells with regard to centrifugation, the wash and dilution process prior to the experiments. Figure 5-5 shows impedance measurements of average cell transparency using PS beads and of algae incubated in media of different salinities. The transparency was calculated using peak intensity measured at 20 MHz over peak intensity measured at 500 kHz. The mean transparency of PS beads was similar across treatments, whereas the mean transparency values of algal cells under different salt conditions were highly differentiated. Cell transparency decreased as the salinity increased from 0 M to 0.3 M and then increased from 0.3 M to 1.3 M. The moderate salinity level did not impact the property of PS beads and hence bead transparency was unaltered.

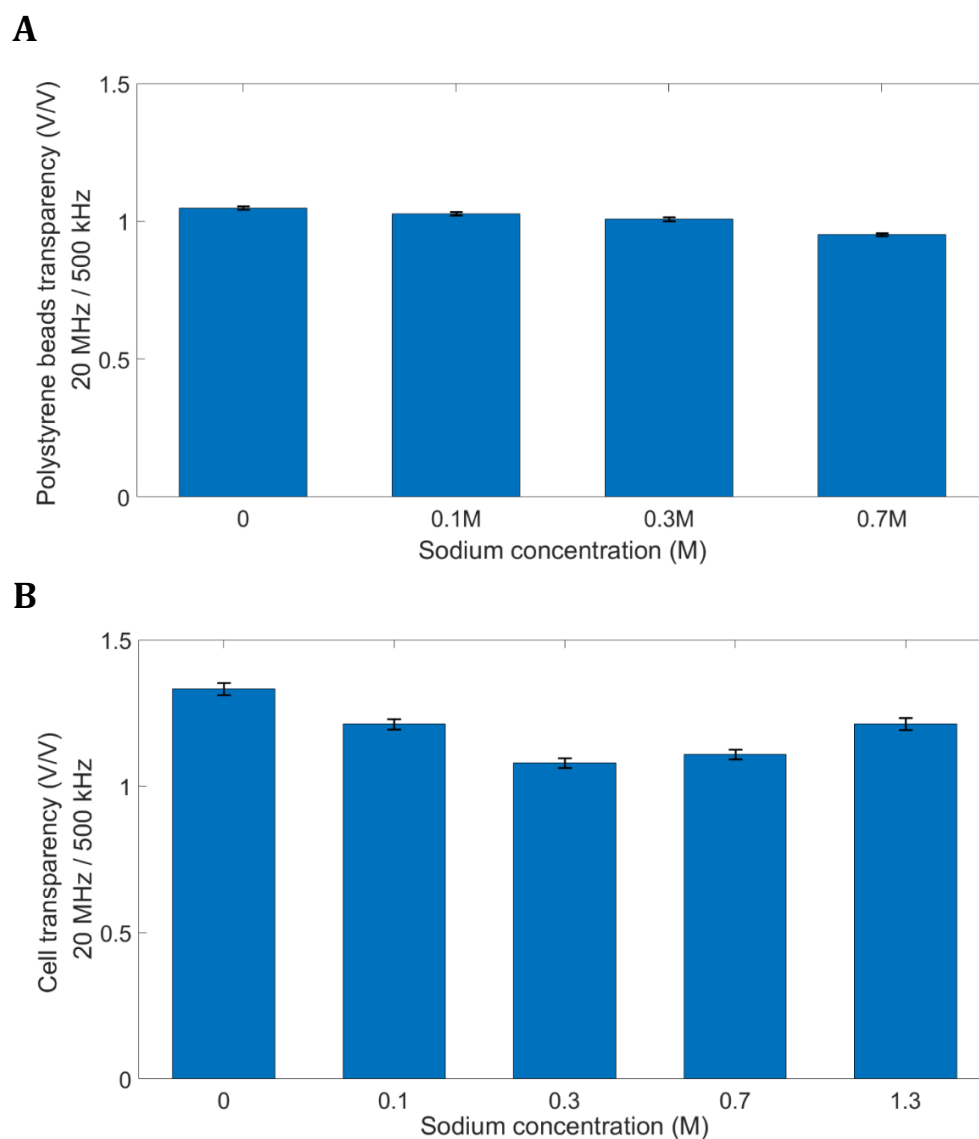


Figure 5-5. Impact of different culture salt conditions on polystyrene bead (PS) and algal cell impedance. A) Average PS bead transparency calculated using peak intensity measured at 20 MHz over peak intensity measured at 500 kHz. B) Average cell transparency calculated using peak intensity measured at 20 MHz over peak intensity measured at 500 kHz.

In contrast, algal cells need to regulate the flow of sodium ions in the different salinity environments to maintain ionic homeostasis [119]. As a result, in addition to changes in cell size, the algal cell membrane and cytoplasm were altered to accommodate the changing environment [120]. This series of responses changed several frequency-

dependent electrical properties of the membrane and the cytoplasm, such as surface conductance, dielectric permittivity, and the charging profile, which had an impact on electrical impedance and cell transparency, that changed accordingly [121]. At a salinity of around 0.3 M NaCl, the algae were apparently able to maintain ionic homeostasis more effectively. Therefore, the membrane ionic permeability was high and resulted in low cell transparency. By comparing the results of PS and algal cells, we validated that our sensor had the ability to detect different levels of algal salt stress using electrical impedance.

Algal cells stressed for different times. We investigated if culturing algal cells in different salinity conditions for different periods of time had an impact on the impedance response. Algal cells were cultured in three different salinity conditions (0.01 M, control: 1 M, and 1.5 M NaCl) and sampled at four different time points (1 h, 5 h, 1 d, and 5 d). Cells cultured in 1 M salinity were used as the control because they grew best in this condition [119]. All samples were washed 3X to remove the residual original medium. We measured the impedance of algal cells using impedance flow cytometry. The cell transparency was calculated as the ratio of peak amplitude at 20 MHz over peak amplitude at 500 kHz. As shown in the average cell transparency (Figure 5-6), cell impedance response in terms of transparency was different at 1 h. The high and low salt groups were significantly less transparent than the control group. Cells in these two groups presumably were more highly stressed in the short-term and the membrane became less permeable with respect to ion transport. After 5 hours, and up to 1 day, cells adapted better to the environment and thus membrane permeability

again normalized. Hence, cells were more transparent to the surrounding environment and the electric field generated by the electrodes. After 5 days, the high salt group could not recover from the long-term salinity stress and growth of these cells was greatly diminished [119]. Therefore, the cytoplasm of this group was less conductive and cells become less transparent when compared to the other two groups.

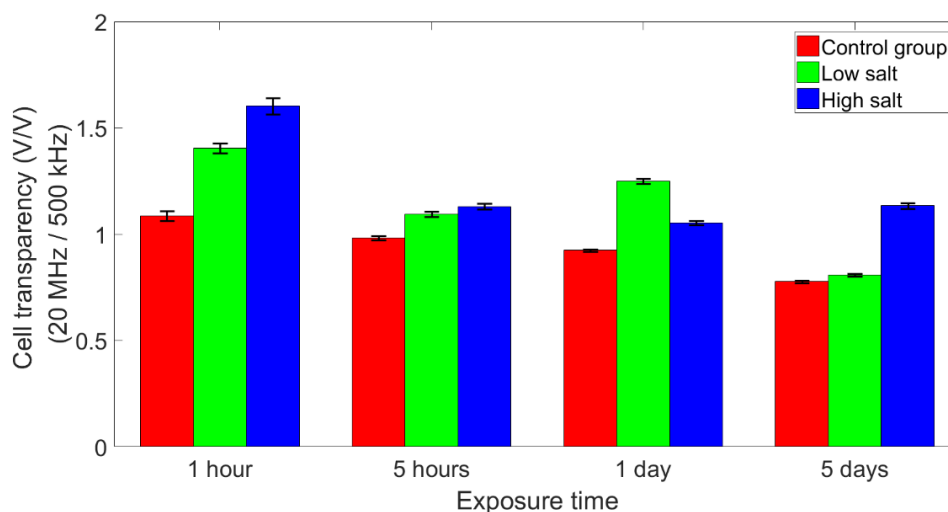


Figure 5-6. Impact of time on algal cell impedance. The plot shows the average cell transparency calculated using peak intensity measured at 20 MHz over peak intensity measured at 500 kHz.

Figure 5-7 shows the impedance scatter plot of individual algal cells cultured in different salinity media for 1 h, 5 h, 1 d, and 5 d. The solid line is the average cell transparency in terms of size. The impedance peak intensity of algal cell at 500 kHz illustrates cell size. The second x-axis on the top of the images shows the corresponding cell size, which was determined through light microscopy. The peak intensity at 5 MHz indicates ionic permeability of the cell membrane [83]. At 1 h, cells under low or high salt stress alter their membrane to be less permeable than cells in the control group

while maintaining a similar size to withstand the shock. After 5 h and 1 d, all cells in different media had similar properties, except the low salt group, which had a slightly larger size. However, on day 5 cells under both high salt and low salt conditions were less well adapted and showed a similar, relatively high permeability with low salt conditions cells having a larger cell size. The membrane of cells in both conditions was more permeable than that of cells in the control medium. Outliers in the data scatter plot were of interest because they represent phenotypes such as algae that have the ability to maintain cell size and/or membrane ionic permeability under prolonged salt stress. For example, the outlier cells marked with black circles maintain relatively high permeability and large cell size under both low and high salt conditions after the 5-day exposure. With the addition of an integrated sorter, our device potentially could be used to isolate cells with specific impedance properties for downstream analysis.

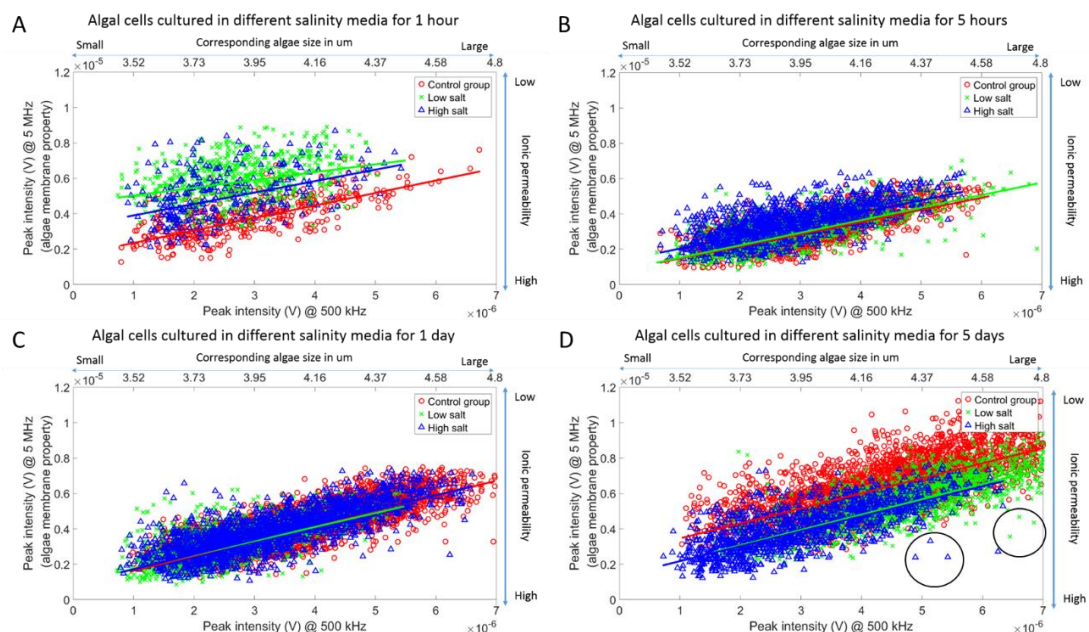


Figure 5-7. The impedance scatter of individual algal cells cultured in different salinity media for 1h (a), 5h (b), 1d (c), and 5d (d).

5.3. Discussion and conclusion

Picochlorum SE3 is a remarkably versatile coccoid green alga that can tolerate a wide salinity range [122]. Strategies for maintaining ionic homeostasis are critical for the survival of *Picochlorum* SE3 in its natural habitat of a brackish water coastal lagoon that is subject to large fluctuations in salinity through evaporation, precipitation, and tidal influx of seawater. The San Elijo Lagoon system in California where this strain was isolated has salinities that range from 108.3‰ in the dry season to freshwater levels (1.7‰) in the rainy winter season. Nutrients such as phosphate, nitrate, nitrite, and ammonium also show extreme variation. *Picochlorum* SE3 is present year-round in this fluctuating environment and therefore has evolved mechanisms to deal with this long-term stress. For example, this alga encodes six copies of the AtNHX8/salt overly sensitive 1 (SOS1) gene (compared to one in the marine green alga *Ostreococcus tauri*) and contains several horizontally transferred bacterial genes that play roles in abiotic stress responses [118, 119]. The overall “genetic toolkit” (e.g., transcriptomic response) that *Picochlorum* SE3 deploys to survive salt stress is however shared by many other algae and plants and is well understood [123-125].

Nonetheless, without analyzing impedance phenotypes associated with different gene knockouts, we have no direct way to connect cell impedance with genetic or transcriptomic data. Therefore, the inferences we make about how electrical impedance intersects with algal biology are speculative but broadly consistent with existing physiological and RNA-seq results from *Picochlorum* SE3 [68, 118, 119]. Specifically, the growth rate of this alga, when pre-conditioned to 1 M NaCl peaks at 100 mM NaCl and is reduced drastically as the culture salinity is increased above 1M NaCl. Analysis

of the cultures shows that the PSII quantum efficiency (proportional to F_v/F_m) is lessened in the short-term (2 h) at both lower and higher salt concentrations. The correlation of F_v/F_m and the growth rate, based on salt conditions after 24 h suggests that energy resources normally devoted to growth are instead used to maintain osmotic balance, with both low and high salinity having an impact [119]. Higher observed growth rates under low salt indicates that these conditions favor enhanced growth after an initial acclimation period, whereas high salt stress does not allow recovery of the growth rate over the longer-term (up to several days; for more details, see [119]). Finally, an intriguing finding in our study is the strict control of cell size apparent in control populations as well as in the different salt treatments that ranges from 4.5-4.8 μm (Figure 5-7). Even after 5 d when the low and high salt populations have differentiated in terms of cell size, they remain within the bounds formed by the control group (Figure 5-7D). These results suggest that cell size is “hard-wired” in *Picochlorum* SE3 and that cells explore (and not escape) the range of possible sizes under different salt conditions.

In this work, we presented the use of electrical impedance as an indicator of cell health and for identifying specific microalgal phenotypes by implementing multi-frequency impedance flow cytometry. Multi-frequency impedance responses provide information about the size and membrane and cytoplasm ionic permeability of algal cells. These properties will change as cells undergo salt stress for different time periods. Large cell size exhibits a large impedance response at lower frequency (~ 500 kHz) [83]. High ionic permeability produces a small impedance response at higher frequency (> 5 MHz). By investigating the impedance at different frequencies, we were able to resolve

differences in cell size, infer membrane and cytoplasm ionic permeability, identify outliers in the cell population distribution, and estimate the overall level of cell stress. Our method provides a novel high-throughput approach to study algal (and potentially, any microbial) cell health. In addition, this approach can be used to identify and sort desired (e.g., experimentally evolved, mutant) cell phenotypes based on their electrical impedance.

Several optimization steps could be made to the device to further improve the accuracy of this method for identifying and sorting cell phenotypes. Implementing multi-electrodes for differential configuration can remove some of the interference and noise from the environment during measurement, such as the baseline shift and white noise, and thus can enhance the signal to noise ratio. Incorporating temperature sensors in the microfluidic channel can correct day-to-day variation due to temperature differences that can affect conductivity of the medium and hence cell impedance. These advances could also reduce the number of algal cells used for analysis and the testing time. In summary, our method captures impedance changes in the microfluidic channel and relies on a portable readout instrument, which can also be integrated on a chip to further minimize the size in future iterations. Impedance flow cytometry enables measuring hundreds of cells in minutes to save analysis time. Moreover, it requires small sample volumes and no complex sample preparation process. Given these advantages, our method provides an opportunity for the rapid *in situ* analysis of cell phenotype, and in the future, sorting of cells with desired properties.

5.4. Material and Methods

5.4.1 Algal cell preparation

Picochlorum SE3 was cultivated as previously described in artificial seawater [118] based Guillard's f/2 medium [126] without silica (f/2 ASW–Si). The cells were grown at 25 °C under continuous light ($100 \mu\text{E m}^{-2} \text{s}^{-1}$) on a rotary shaker at 100 rpm (Innova 43, New Brunswick Eppendorf).

5.4.2 Device fabrication and integration

The device consists of two pairs of gold electrodes on a glass substrate and a polydimethylsiloxane (PDMS) microfluidic channel fabricated using microfabrication technology. Electrodes were patterned on a 3-inch glass wafer using standard photolithography procedures. The process started with wafer cleaning using acetone, methanol and DI water. Thereafter, a thin layer of positive photoresist (AZ5214, MicroChemicals GmbH) was spin coated on the wafer. After pre-bake, mask and wafer alignment, UV exposure, development and post-bake, the desired pattern was transferred from the mask to the wafer. The metals, 5 nm chromium and 100 nm gold, were deposited sequentially using electron beam evaporation, whereby the chromium layer was used for enhancing the adhesion of gold film on glass. Unintended parts were lifted off by submerging the wafer in acetone. The resultant electrodes were 20 μm in width and the gap between two electrodes was 20 μm . The SU-8 (negative photoresist) silicon mold for microfluidic channel was fabricated using standard soft lithography procedures as described in the literature [65, 115, 127]. The size of the channel is 30

μm in width and $8\mu\text{m}$ in height. The channel pattern was transferred from the mold to a PDMS slab using the following process. Mixed 10:1 PDMS polymer and curing agent (Sylgard 184, Dow Corning) sufficiently. Then, poured the mixture onto the channel mold, degassed to remove bubble in the mixture and baked at 80°C for 30 minutes to allow for curing. Afterwards, the PDMS channel was peeled off and two holes were punched through the PDMS to be used as inlet reservoir (5 mm in diameter) and outlet reservoir (1.2 mm in diameter). The microfluidic channel and the electrodes on glass substrate were covalently bonded by treating the two surfaces with oxygen plasma.

5.4.3 Multi-frequency impedance flow cytometry

Multi-frequency impedance flow cytometry was done to capture the impedance response of algal cells at 8 different frequencies, ranging from 500 kHz to 30 MHz. The algal cells were initially cultured in Guillard's f/2 medium emended with different NaCl amounts (0 M, 0.01 M, 0.1 M, 0.3 M, 0.7 M, 1 M, 1.3 M, and 1.5 M) for different time periods (1 hour, 5 hours, 1 day, and 5 days) and then analyzed. Cells in 3 mL of the original culture were sampled, spun down and the culture buffer was replaced with 1x phosphate buffered saline (PBS). Samples were washed in PBS 3 times to remove the original culture buffer. Finally, samples were diluted in 50 μL PBS, which provided a continuous flow in the cytometry experiment for more than 15 min without using a noisy syringe pump. The impedance flow cytometry started with making the microfluidic channel hydrophilic by implementing an oxygen plasma treatment. The PBS was injected into the channel to preserve the hydrophilicity until the measurement started. Fluid was driven by capillary force, and the pressure gradient induced by the

fluid height difference between inlet and outlet. PBS was withdrawn from the channel and algal cells were introduced from the inlet. The impedance across two electrodes was changed when a cell flowed through the sensing region, because the electrical field was blocked by the cell. The impedance changes at 8 different frequencies were captured by a commercial lock-in amplifier (Zurich Instruments HF2A, Zurich, Switzerland). A superposition of 8 different frequency AC signals generated by the same lock-in amplifier was used to excite the electrodes. The data were demodulated, then sent to a local computer and analyzed using MATLAB (MathWorks, Natick, MA, USA). To minimize the impact of noise and interference from the environment on impedance measurement, the device was placed in a metal box during the experiment.

Chapter 6: Bacterial phenotype characterization based on electrical impedance signature

6.1 Introduction

In this project, we present a method to characterize bacterial phenotype using electrical impedance cytometry at multiple frequencies, which provides bacteria dielectric properties at the single cell level. We investigated the frequency-dependent impedance of *Staphylococcus aureus* (*S. aureus*). Similar to what we did in the previous project [128], different phenotypic bacteria were cultured overnight started with similar concentration and sampled at three different time points. The impedance was measured over a frequency range using a multi-frequency lock-in amplifier in conjunction with an electrical impedance sensor. We demonstrate the bacterial phenotype could be characterized based on their electrical impedance.

6.2. Materials and Methods

6.2.1 Bacterial strains

S. aureus strains were cultured in TSB overnight and grown at 37°C with shaking at 200 rpm. Cells were cultured in 10 ml capacity culture tubes containing 1 of liquid medium. The chemically defined minimal medium was described previously and was supplemented with 0.5 µg/ml of lipoic acid.

6.2.2 Device fabrication and integration

The device consists of two layers, a pair of gold electrodes deposited on a glass wafer and a polydimethylsiloxane (PDMS) microfluidic channel. We used the standard photolithography technique to pattern electrodes onto a glass wafer. The wafer was cleaned using acetone, methanol, and DI water. Then, a thin layer of positive photoresist (AZ5214, MicroChemicals GmbH) was spin-coated on the wafer. After pre-bake, mask and wafer alignment, UV exposure, development, and post-bake, the desired pattern was transferred from the photomask to the wafer. 5 nm chromium and 100 nm gold were deposited sequentially using electron beam evaporation. The chromium layer was used for enhancing the adhesion of gold film on the glass. At last, the wafer was submerged in acetone to remove unintended parts. The fabricated electrodes were 20 μm in width, and the gap between the two electrodes was 20 μm . The fabrication of the PDMS microfluidic channel included two parts. First, the SU-8 (negative photoresist) silicon mold for the microfluidic channel was fabricated using standard soft lithography procedures. The size of the channel is 30 μm in width and 8 μm in height. Second, the channel pattern was transferred from the mold to a PDMS slab using the following process. Mixed 10:1 PDMS polymer and curing agent (Sylgard 184, Dow Corning) sufficiently. Then, poured the mixture onto the channel mold, degassed to remove the bubble, and baked at 80°C for 30 minutes to allow for curing. Afterward, the PDMS channel was peeled off and two holes were punched through the PDMS to be used as an inlet reservoir (5 mm in diameter) and outlet reservoir (1.2 mm in diameter). The microfluidic channel and the electrodes on the glass substrate were firmly bonded by treating the two surfaces with oxygen plasma.

6.2.3 Multi-frequency impedance flow cytometry

We captured the impedance responses of bacteria cells at four different frequencies using multi-frequency impedance flow cytometry. The bacterial cells were initially cultured in tryptic soy broth (TSB) overnight and then analyzed. Cells in 2 mL of the original culture were sampled. Samples were washed in 1x phosphate-buffered saline (PBS) 3 times to remove the residue of TSB. Finally, samples were diluted in 50 μ L PBS to flow in the cytometry experiment for more than 15 min without using a pump. The impedance flow cytometry began with making the microfluidic channel hydrophilic by treating it with oxygen plasma. The PBS was injected into the channel to preserve the hydrophilicity. The fluid was driven by capillary force, and the pressure gradient induced by the fluid height difference between inlet and outlet. After withdrawing PBS in the channel inlet, bacteria cells were added to the inlet. The impedance across two electrodes was changed when a cell flowed through the sensing region because the electrical field was blocked by the cell. A commercial lock-in amplifier (Zurich Instruments HF2A, Zurich, Switzerland) was used to capture the impedance change in the sensing region at 4 different frequencies. The signals were demodulated by the lock-in amplifier and then sent to a local computer for analysis using MATLAB (MathWorks, Natick, MA, USA). To reduce the noise and interference from the environment, the device was placed in a metal box during the experiment.

6.3 Results and discussions

6.3.1 Impedance analysis of bacterial cell viability

Initially, we studied the impedance responses of live and dead *S. aureus* cells. The bacteria were killed by treating them with heat at 100°C for 20 minutes. Multi-frequency impedance flow cytometry was performed to measure the impedance of cells. Both live and dead cells were washed with 1X phosphate buffered saline (PBS) three times and then diluted in 50 μ L of PBS immediately before the measurement to allow higher sensitivity. The results of these analyses are shown in Figure 6-1. As apparent in the figure, the average impedance of live cells was greater than that of dead cells over all measured frequencies. These results indicate that dead cells are more transparent to the surrounding electric field, because ions in the media can flow more freely through the membrane. Cells exhibit larger impedance at 500 kHz and the impedance decreases as the frequency increases. It implies that the capacitance of the membrane is getting shorted gradually and the cytoplasm conductance is more involved, which results in a smaller impedance displayed at higher frequencies.

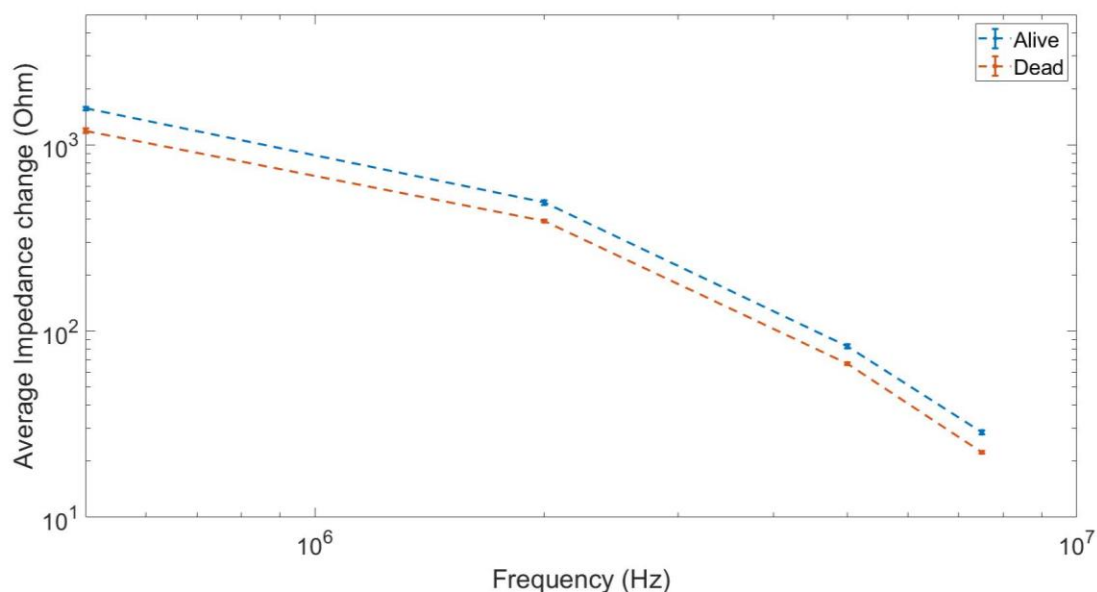


Figure 6-1. Impedance spectra of alive and dead cells. The impedance was measured at 500 kHz, 2 MHz, 5 MHz, and 7.5 MHz. The dot line shows the trend of impedance change as frequency increases.

6.3.2 Bacterial phenotype characterization

We investigate the electrical impedance signature of three different bacterial phenotypes, wild type, HemB mutant and MenD mutant using multi-frequency impedance flow cytometry. HemB mutants and MenD mutants lack of the gene involved in biosynthesis of heme and menadione respectively. Heme and menaquinone are important for the electron transport the respiratory chain to both oxygen and nitrate [117]. For this approach, 2 mL of bacteria cells were centrifuged, washed three times with 1X PBS and diluted in 50 μ L PBS. Figure 6-2 shows the average impedance spectra of different phenotypic bacteria. All cells follow the same trend that as frequency increases the impedance of cells decreases. The wild type bacteria have the lowest impedance over the frequency range compared with HemB mutants and MenD

Mutant. HemB mutant is closer to MenD mutant, which indicates that the menD mutant is similar to that of the hemB mutant. MenD mutants have larger impedance compared with HemB mutants. It implies that the carbon metabolism was more profoundly affected in the menD mutant [118].

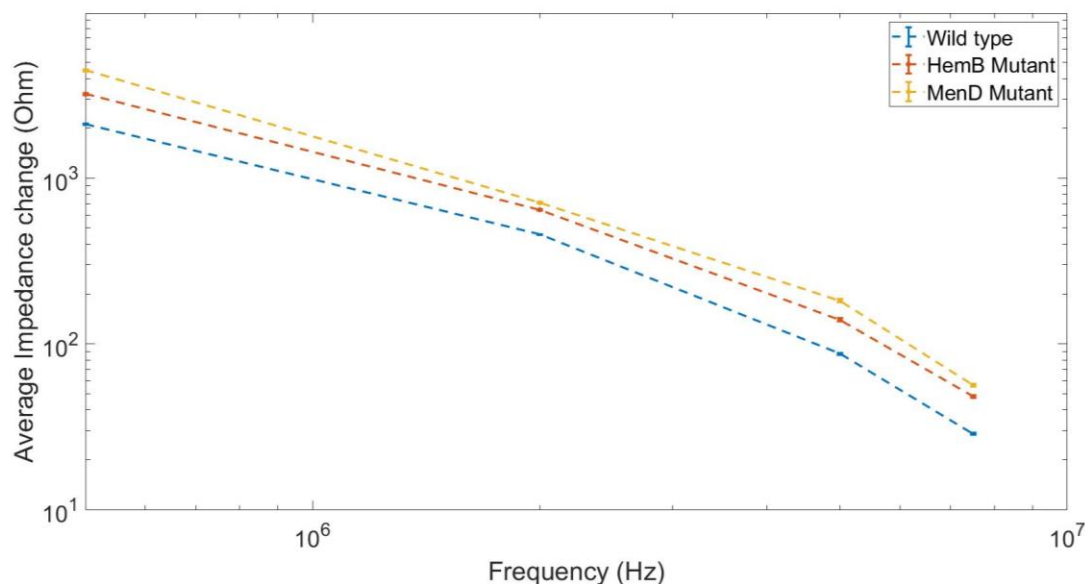


Figure 6-2. Impedance spectra of different phenotypic bacteria (Wild type, HemB mutant and MenD mutant). The impedance was measured at 500 kHz, 2 MHz, 5 MHz, and 7.5 MHz. The dot line shows the trend of impedance change as frequency increases.

In this study, we showed that using impedance flow cytometry we could differentiate alive and dead bacteria cells. Furthermore, different phenotypic bacteria could be characterized based on their electrical impedance response. Our method provides a novel high-throughput approach to study bacterial cell and potentially could be used for antimicrobial susceptibility test. Besides, the detection process reduces the turnover time to only 15 minutes.

Chapter 7: Conclusions

In this thesis, we present the use of multi-frequency impedance cytometry on DNA quantification and sizing, multiplex barcodes detection and microbial phenotype characterization. We build a platform to perform impedance cytometry, which consists of a microfluidic channel made of polydimethylsiloxane (PDMS), and a pair of electron beam-deposited reusable coplanar gold electrodes on a fused silica substrate. The dimension of the microfluidic channel is optimized according to the size of sample to be tested to obtain the best signal to noise ratio. Our impedance sensor in combination with microfluidics technology could potentially be designed for multiplex and portable applications. Impedance cytometry enables measuring hundreds of beads or cells in minutes to save analysis time. Moreover, it requires small sample volumes and no complex sample preparation process. Given these advantages, multi-frequency impedance cytometry provides an opportunity for the rapid *in situ* analysis.

To quantify DNA amount and size DNA length, we coupled DNA fragments onto paramagnetic beads and measured the impedance at different frequencies using multi-frequency impedance cytometry. We show that DNA binding can be detected through frequency-dependent impedance peak response. IPR differed between DNA coated beads and bare streptavidin coated beads (negative control) as DNA concentration increased in the linear region of the dynamic range. We show the utility of this new technology for reliable detection of DNA fragments of different concentrations and lengths. Our experiments provide an approach to quantify DNA fragments at high accuracy and precision at the femtomolar level and over a 100-fold dynamic range. Furthermore, we also demonstrate that without using beads, we could differentiate

different length DNA based on their bulk impedance responses. It further decreases the sample preparation time. The results of blinded experiments indicates that we could accurately predicted the length of DNA in the sample.

For multiplex barcodes fabrication, we deposit different thicknesses and types of oxide layers on top of bare polystyrene beads and fabricate 9 different barcoded particles. The impedance signature of each barcodes could be captured by multi-frequency impedance cytometry. We demonstrate the single layer of oxide could sufficiently modulate the frequency dependent impedance and thus eliminate the need for the intermediate gold layer and simplify fabrication. By implementing impedance measurements at multiple frequencies in conjunction with machine learning analysis, we demonstrate the capability of our sensor to detect different particle barcodes. As a result, these particles can be selected and utilized as barcodes in a functional biomarker assay to improve the throughput in the future.

We studied the microalgal health under different salt stress using multi-frequency impedance flow cytometry. Results show that electrical impedance could be used as an indicator of cell health and for identifying specific microalgal phenotypes. Multi-frequency impedance responses provide information about the size and membrane and cytoplasm ionic permeability of algal cells. These properties will change as cells undergo salt stress for different time periods. By investigating the impedance at different frequencies, we are able to resolve differences in cell size, infer membrane and cytoplasm ionic permeability, identify outliers in the cell population distribution, and estimate the overall level of cell stress. Our method provides a novel high-throughput approach to study algal (and potentially, any microbial) cell health. In

addition, this approach can be used to identify and sort desired (e.g., experimentally evolved, mutant) cell phenotypes based on their electrical impedance.

To characterize microbial phenotype, we investigated the impedance of different phenotypes of *Staphylococcus Aureus* using impedance flow cytometry. Results demonstrated that electrical impedance could be used for identifying specific bacterial phenotypes. Different mutants were differentiated based on their distinct impedance responses. Our method provides a novel high-throughput approach to study bacterial cells and potentially can be used for antimicrobial susceptibility test.

The results of this study have been published and presented in following journals and conferences:

Journal papers:

Sui, J., Foflonker, F., Bhattacharya, D., & Javanmard, M. (2020). Electrical impedance as an indicator of microalgal cell health. *Scientific reports*, 10(1), 1-9.

Sui, J., Xie, P., Lin, Z., & Javanmard, M. (2020). Electronic classification of barcoded particles for multiplexed detection using supervised machine learning analysis. *Talanta*, 120791.

Conferences:

Sui, J., Xie, P., Lin, Z., & Javanmard, M. (2018, January). Multiplexed molecular biomarker analysis using an expanded library of nanoelectronically barcoded particles enabled through machine learning analysis. In *2018 IEEE Micro Electro Mechanical Systems (MEMS)* (pp. 444-447). IEEE.

Sui, J., Gandotrab, N., Xie, P., Lin, Z., Scharfe, C., & Javanmard, M. DNA Sizing and Quantification Using Multi-Frequency Impedance Cytometry. 2018 MRS Fall Meeting.

Sui, J., Xie, P., Lin, Z., & Javanmard, M. Electronically Barcoded Particles For Multiplexed Molecular Bioanalysis: A Study Of The Effect Of Thin Film Dielectric Permittivity And Thickness. *Proceedings of MicroTAS 2017*.

Sui, J., Gandotrab, N., Xie, P., Lin, Z., Scharfe, C., & Javanmard, M. Label-free DNA Quantification By Multi-frequency Impedance Cytometry And Machine Learning Analysis. *Proceedings of MicroTAS 2017*.

References:

- [1] K. Hsieh, B. S. Ferguson, M. Eisenstein, K. W. Plaxco, and H. T. Soh, "Integrated electrochemical microsystems for genetic detection of pathogens at the point of care," *Accounts of chemical research*, vol. 48, no. 4, pp. 911-920, 2015.
- [2] W. Su, X. Gao, L. Jiang, and J. Qin, "Microfluidic platform towards point-of-care diagnostics in infectious diseases," *Journal of Chromatography A*, vol. 1377, pp. 13-26, 2015.
- [3] A. N. Glazer and H. S. Rye, "Stable dye-DNA intercalation complexes as reagents for high-sensitivity fluorescence detection," *Nature*, vol. 359, no. 6398, p. 859, 1992.
- [4] F. Zhou and B. Li, "Exonuclease III-assisted target recycling amplification coupled with liposome-assisted amplification: one-step and dual-amplification strategy for highly sensitive fluorescence detection of DNA," *Analytical chemistry*, vol. 87, no. 14, pp. 7156-7162, 2015.
- [5] F. Degliangeli, P. Kshirsagar, V. Brunetti, P. P. Pompa, and R. Fiammengio, "Absolute and direct microRNA quantification using DNA-gold nanoparticle probes," *Journal of the American Chemical Society*, vol. 136, no. 6, pp. 2264-2267, 2014.
- [6] J. N. Anker, W. P. Hall, O. Lyandres, N. C. Shah, J. Zhao, and R. P. Van Duyne, "Biosensing with plasmonic nanosensors," in *Nanoscience And Technology: A Collection of Reviews from Nature Journals*: World Scientific, 2010, pp. 308-319.
- [7] X. Fu, Z. Cheng, J. Yu, P. Choo, L. Chen, and J. Choo, "A SERS-based lateral flow assay biosensor for highly sensitive detection of HIV-1 DNA," *Biosensors and Bioelectronics*, vol. 78, pp. 530-537, 2016.
- [8] S. Kim, J. M. Kim, J. E. Park, and J. M. Nam, "Nonnoble - Metal - Based Plasmonic Nanomaterials: Recent Advances and Future Perspectives," *Advanced Materials*, p. 1704528.
- [9] X. Cui *et al.*, "Lensless high-resolution on-chip optofluidic microscopes for *Caenorhabditis elegans* and cell imaging," *Proceedings of the National Academy of Sciences*, vol. 105, no. 31, pp. 10670-10675, 2008.
- [10] S. Pang, X. Cui, J. DeModena, Y. M. Wang, P. Sternberg, and C. Yang, "Implementation of a color-capable optofluidic microscope on a RGB CMOS color sensor chip substrate," *Lab on a Chip*, vol. 10, no. 4, pp. 411-414, 2010.
- [11] S. O. Isikman *et al.*, "Lens-free optical tomographic microscope with a large imaging volume on a chip," *Proceedings of the National Academy of Sciences*, 2011.
- [12] Q. Wei *et al.*, "Imaging and sizing of single DNA molecules on a mobile phone," *ACS nano*, vol. 8, no. 12, pp. 12725-12733, 2014.

- [13] I. Navruz *et al.*, "Smart-phone based computational microscopy using multi-frame contact imaging on a fiber-optic array," *Lab on a Chip*, vol. 13, no. 20, pp. 4015-4023, 2013.
- [14] Y. Rivenson *et al.*, "Deep learning enhanced mobile-phone microscopy," *ACS Photonics*, vol. 5, no. 6, pp. 2354-2364, 2018.
- [15] N. Talukder *et al.*, "A portable battery powered microfluidic impedance cytometer with smartphone readout: towards personal health monitoring," *Biomedical microdevices*, vol. 19, no. 2, p. 36, 2017.
- [16] G. Liu *et al.*, "A carbon nanotube-based high-sensitivity electrochemical immunosensor for rapid and portable detection of clenbuterol," *Biosensors and Bioelectronics*, vol. 28, no. 1, pp. 308-313, 2011.
- [17] Y. Temiz and E. Delamarche, "Sub-nanoliter, real-time flow monitoring in microfluidic chips using a portable device and smartphone," *Scientific reports*, vol. 8, no. 1, p. 10603, 2018.
- [18] A. Gholizadeh *et al.*, "Toward point-of-care management of chronic respiratory conditions: Electrochemical sensing of nitrite content in exhaled breath condensate using reduced graphene oxide," *Microsystems & Nanoengineering*, vol. 3, p. 17022, 2017.
- [19] W. Gao *et al.*, "Fully integrated wearable sensor arrays for multiplexed in situ perspiration analysis," *Nature*, vol. 529, no. 7587, p. 509, 2016.
- [20] A. Furniturewalla, M. Chan, J. Sui, K. Ahuja, and M. Javanmard, "Fully integrated wearable impedance cytometry platform on flexible circuit board with online smartphone readout," *Microsystems & Nanoengineering*, vol. 4, no. 1, p. 20, 2018.
- [21] Y. Xiao, A. A. Lubin, B. R. Baker, K. W. Plaxco, and A. J. Heeger, "Single-step electronic detection of femtomolar DNA by target-induced strand displacement in an electrode-bound duplex," *Proceedings of the National Academy of Sciences*, vol. 103, no. 45, pp. 16677-16680, 2006.
- [22] C. Singhal, M. Khanuja, N. Chaudhary, C. Pundir, and J. Narang, "Detection of chikungunya virus DNA using two-dimensional MoS₂ nanosheets based disposable biosensor," *Scientific reports*, vol. 8, no. 1, p. 7734, 2018.
- [23] Y. Yan, S. Ding, D. Zhao, R. Yuan, Y. Zhang, and W. Cheng, "Direct ultrasensitive electrochemical biosensing of pathogenic DNA using homogeneous target-initiated transcription amplification," *Scientific reports*, vol. 6, p. 18810, 2016.
- [24] C. Gao, Z. Guo, J.-H. Liu, and X.-J. Huang, "The new age of carbon nanotubes: An updated review of functionalized carbon nanotubes in electrochemical sensors," *Nanoscale*, vol. 4, no. 6, pp. 1948-1963, 2012.
- [25] H. Peng, L. Zhang, C. Soeller, and J. Travas-Sejdic, "Conducting polymers for electrochemical DNA sensing," *Biomaterials*, vol. 30, no. 11, pp. 2132-2148, 2009.
- [26] L. Xia, Z. Wei, and M. Wan, "Conducting polymer nanostructures and their application in biosensors," *Journal of colloid and interface science*, vol. 341, no. 1, pp. 1-11, 2010.

- [27] H. Y. Lau, H. Wu, E. J. Wee, M. Trau, Y. Wang, and J. R. Botella, "Specific and sensitive isothermal electrochemical biosensor for plant pathogen DNA detection with colloidal gold nanoparticles as probes," *Scientific reports*, vol. 7, p. 38896, 2017.
- [28] Y. Shao, J. Wang, H. Wu, J. Liu, I. A. Aksay, and Y. Lin, "Graphene based electrochemical sensors and biosensors: a review," *Electroanalysis: An International Journal Devoted to Fundamental and Practical Aspects of Electroanalysis*, vol. 22, no. 10, pp. 1027-1036, 2010.
- [29] B. Li, G. Pan, N. D. Avent, R. B. Lowry, T. E. Madgett, and P. L. Waines, "Graphene electrode modified with electrochemically reduced graphene oxide for label-free DNA detection," *Biosensors and Bioelectronics*, vol. 72, pp. 313-319, 2015.
- [30] J. S. Daniels and N. Pourmand, "Label - free impedance biosensors: Opportunities and challenges," *Electroanalysis*, vol. 19, no. 12, pp. 1239-1257, 2007.
- [31] H. Ma *et al.*, "An impedance-based integrated biosensor for suspended DNA characterization," *Scientific reports*, vol. 3, p. 2730, 2013.
- [32] Z. Lin, X. Cao, P. Xie, M. Liu, and M. Javanmard, "PicoMolar level detection of protein biomarkers based on electronic sizing of bead aggregates: theoretical and experimental considerations," *Biomedical microdevices*, vol. 17, no. 6, p. 119, 2015.
- [33] A. Numnuam *et al.*, "Capacitive biosensor for quantification of trace amounts of DNA," *Biosensors and Bioelectronics*, vol. 24, no. 8, pp. 2559-2565, 2009.
- [34] R. Vogel *et al.*, "High-resolution single particle zeta potential characterisation of biological nanoparticles using tunable resistive pulse sensing," *Scientific reports*, vol. 7, no. 1, p. 17479, 2017.
- [35] C. A. Merchant *et al.*, "DNA translocation through graphene nanopores," *Nano letters*, vol. 10, no. 8, pp. 2915-2921, 2010.
- [36] J. Shim *et al.*, "Nanopore-based assay for detection of methylation in double-stranded DNA fragments," *ACS nano*, vol. 9, no. 1, pp. 290-300, 2015.
- [37] B. M. Venkatesan and R. Bashir, "Nanopore sensors for nucleic acid analysis," *Nature nanotechnology*, vol. 6, no. 10, p. 615, 2011.
- [38] L. Esfandiari, M. Lorenzini, G. Kocharyan, H. G. Monbouquette, and J. J. Schmidt, "Sequence-Specific DNA Detection at 10 fM by Electromechanical Signal Transduction," *Analytical chemistry*, vol. 86, no. 19, pp. 9638-9643, 2014.
- [39] O. A. Saleh and L. L. Sohn, "Direct detection of antibody-antigen binding using an on-chip artificial pore," *Proceedings of the National Academy of Sciences*, vol. 100, no. 3, pp. 820-824, 2003.
- [40] B. Laxman *et al.*, "A first-generation multiplex biomarker analysis of urine for the early detection of prostate cancer," *Cancer research*, vol. 68, no. 3, pp. 645-649, 2008.

- [41] N. R. Kitteringham, R. E. Jenkins, C. S. Lane, V. L. Elliott, and B. K. Park, "Multiple reaction monitoring for quantitative biomarker analysis in proteomics and metabolomics," *Journal of Chromatography B*, vol. 877, no. 13, pp. 1229-1239, 2009.
- [42] Y. Li *et al.*, "Circular RNA is enriched and stable in exosomes: a promising biomarker for cancer diagnosis," *Cell research*, vol. 25, no. 8, p. 981, 2015.
- [43] H. Gao *et al.*, "High-throughput screening using patient-derived tumor xenografts to predict clinical trial drug response," *Nature medicine*, vol. 21, no. 11, p. 1318, 2015.
- [44] D. R. Rhodes, M. G. Sanda, A. P. Otte, A. M. Chinnaiyan, and M. A. Rubin, "Multiplex biomarker approach for determining risk of prostate-specific antigen-defined recurrence of prostate cancer," *Journal of the National Cancer Institute*, vol. 95, no. 9, pp. 661-668, 2003.
- [45] J.-H. Kang, H. Vanderstichele, J. Q. Trojanowski, and L. M. Shaw, "Simultaneous analysis of cerebrospinal fluid biomarkers using microsphere-based xMAP multiplex technology for early detection of Alzheimer's disease," *Methods*, vol. 56, no. 4, pp. 484-493, 2012.
- [46] S. Chutipongtanate and K. D. Greis, "Multiplex Biomarker Screening Assay for Urinary Extracellular Vesicles Study: A Targeted Label-Free Proteomic Approach," *Scientific reports*, vol. 8, no. 1, p. 15039, 2018.
- [47] Y. Leng, K. Sun, X. Chen, and W. Li, "Suspension arrays based on nanoparticle-encoded microspheres for high-throughput multiplexed detection," *Chemical Society Reviews*, vol. 44, no. 15, pp. 5552-5595, 2015.
- [48] M. Seydack, "Nanoparticle labels in immunosensing using optical detection methods," *Biosensors and Bioelectronics*, vol. 20, no. 12, pp. 2454-2469, 2005.
- [49] B. J. Battersby, G. A. Lawrie, A. P. Johnston, and M. Trau, "Optical barcoding of colloidal suspensions: applications in genomics, proteomics and drug discovery," *Chemical Communications*, no. 14, pp. 1435-1441, 2002.
- [50] Y. Zhao, H. C. Shum, H. Chen, L. L. Adams, Z. Gu, and D. A. Weitz, "Microfluidic generation of multifunctional quantum dot barcode particles," *Journal of the American Chemical Society*, vol. 133, no. 23, pp. 8790-8793, 2011.
- [51] K. Braeckmans, S. C. De Smedt, C. Roelant, M. Leblans, R. Pauwels, and J. Demeester, "Encoding microcarriers by spatial selective photobleaching," *Nature materials*, vol. 2, no. 3, p. 169, 2003.
- [52] H. Lee, J. Kim, H. Kim, J. Kim, and S. Kwon, "Colour-barcoded magnetic microparticles for multiplexed bioassays," *Nature materials*, vol. 9, no. 9, p. 745, 2010.
- [53] H. Li and X. Sun, "Fluorescence-enhanced nucleic acid detection: using coordination polymer colloids as a sensing platform," *Chemical Communications*, vol. 47, no. 9, pp. 2625-2627, 2011.
- [54] B. J. Battersby, D. Bryant, W. Meutermans, D. Matthews, M. L. Smythe, and M. Trau, "Toward larger chemical libraries: encoding with fluorescent

- colloids in combinatorial chemistry," *Journal of the American Chemical Society*, vol. 122, no. 9, pp. 2138-2139, 2000.
- [55] J. M. Klostranec *et al.*, "Convergence of quantum dot barcodes with microfluidics and signal processing for multiplexed high-throughput infectious disease diagnostics," *Nano letters*, vol. 7, no. 9, pp. 2812-2818, 2007.
 - [56] M. A. Walling, J. A. Novak, and J. R. Shepard, "Quantum dots for live cell and in vivo imaging," *International journal of molecular sciences*, vol. 10, no. 2, pp. 441-491, 2009.
 - [57] Y. Zhao *et al.*, "Quantum - dot - tagged bioresponsive hydrogel suspension array for multiplex label - free DNA detection," *Advanced Functional Materials*, vol. 20, no. 6, pp. 976-982, 2010.
 - [58] N. Hildebrandt, "Biofunctional quantum dots: controlled conjugation for multiplexed biosensors," *Acs Nano*, vol. 5, no. 7, pp. 5286-5290, 2011.
 - [59] S. C. Chapin and P. S. Doyle, "Ultrasensitive multiplexed microRNA quantification on encoded gel microparticles using rolling circle amplification," *Analytical chemistry*, vol. 83, no. 18, pp. 7179-7185, 2011.
 - [60] D. C. Appleyard, S. C. Chapin, R. L. Srinivas, and P. S. Doyle, "Bar-coded hydrogel microparticles for protein detection: synthesis, assay and scanning," *Nature protocols*, vol. 6, no. 11, p. 1761, 2011.
 - [61] M. Y. Liu *et al.*, "Multiplexed analysis of biomarkers related to obesity and the metabolic syndrome in human plasma, using the Luminex-100 system," *Clinical chemistry*, vol. 51, no. 7, pp. 1102-1109, 2005.
 - [62] A. Bhimji *et al.*, "Feasibility of detecting fungal DNA in exhaled breath condensate by the Luminex Multiplex xTAG fungal PCR assay in lung transplant recipients: a pilot study," *The Journal of Heart and Lung Transplantation*, vol. 35, no. 4, p. S37, 2016.
 - [63] H. Cai, T. M.-H. Lee, and I.-M. Hsing, "Label-free protein recognition using an aptamer-based impedance measurement assay," *Sensors and Actuators B: Chemical*, vol. 114, no. 1, pp. 433-437, 2006.
 - [64] B. Kavosi, A. Salimi, R. Hallaj, and F. Moradi, "Ultrasensitive electrochemical immunosensor for PSA biomarker detection in prostate cancer cells using gold nanoparticles/PAMAM dendrimer loaded with enzyme linked aptamer as integrated triple signal amplification strategy," *Biosensors and Bioelectronics*, vol. 74, pp. 915-923, 2015.
 - [65] P. Xie, X. Cao, Z. Lin, and M. Javanmard, "Top-down fabrication meets bottom-up synthesis for nanoelectronic barcoding of microparticles," *Lab on a Chip*, vol. 17, no. 11, pp. 1939-1947, 2017.
 - [66] Z. Wang, M. Gerstein, and M. Snyder, "RNA-Seq: a revolutionary tool for transcriptomics," *Nature reviews genetics*, vol. 10, no. 1, p. 57, 2009.
 - [67] T. Mass *et al.*, "Temporal and spatial expression patterns of biomineralization proteins during early development in the stony coral *Pocillopora damicornis*," *Proc. R. Soc. B*, vol. 283, no. 1829, p. 20160322, 2016.

- [68] F. Foflonker, D. Mollegard, M. Ong, H. S. Yoon, and D. Bhattacharya, "Genomic analysis of *Picochlorum* species reveals how microalgae may adapt to variable environments," *Molecular biology and evolution*, vol. 35, no. 11, pp. 2702-2711, 2018.
- [69] S. V. Puram *et al.*, "Single-cell transcriptomic analysis of primary and metastatic tumor ecosystems in head and neck cancer," *Cell*, vol. 171, no. 7, pp. 1611-1624. e24, 2017.
- [70] R. Vento-Tormo *et al.*, "Single-cell reconstruction of the early maternal-fetal interface in humans," *Nature*, vol. 563, no. 7731, p. 347, 2018.
- [71] S. Li *et al.*, "AC electrokinetics-enhanced capacitive immunosensor for point-of-care serodiagnosis of infectious diseases," *Biosensors and Bioelectronics*, vol. 51, pp. 437-443, 2014.
- [72] K. Wang *et al.*, "Specific membrane capacitance, cytoplasm conductivity and instantaneous Young's modulus of single tumour cells," *Scientific data*, vol. 4, p. 170015, 2017.
- [73] H. S. Kim, T. P. Devarenne, and A. Han, "Microfluidic systems for microalgal biotechnology: a review," *Algal research*, 2017.
- [74] J. C. Jokerst, J. M. Emory, and C. S. Henry, "Advances in microfluidics for environmental analysis," *Analyst*, vol. 137, no. 1, pp. 24-34, 2012.
- [75] P. Mandal, A. Biswas, K. Choi, and U. Pal, "Methods for rapid detection of foodborne pathogens: an overview," *American Journal Of Food Technology*, vol. 6, no. 2, pp. 87-102, 2011.
- [76] L. Yang and R. Bashir, "Electrical/electrochemical impedance for rapid detection of foodborne pathogenic bacteria," *Biotechnology advances*, vol. 26, no. 2, pp. 135-150, 2008.
- [77] E. Bisceglia *et al.*, "A generic and label free method based on dielectrophoresis for the continuous separation of microorganism from whole blood samples," *Sensors and Actuators B: Chemical*, vol. 212, pp. 335-343, 2015.
- [78] P. V. Jones, A. F. DeMichele, L. Kemp, and M. A. Hayes, "Differentiation of *Escherichia coli* serotypes using DC gradient insulator dielectrophoresis," *Analytical and bioanalytical chemistry*, vol. 406, no. 1, pp. 183-192, 2014.
- [79] I. O. K'Owino and O. A. Sadik, "Impedance spectroscopy: a powerful tool for rapid biomolecular screening and cell culture monitoring," *Electroanalysis: An International Journal Devoted to Fundamental and Practical Aspects of Electroanalysis*, vol. 17, no. 23, pp. 2101-2113, 2005.
- [80] K. Cheung, S. Gawad, and P. Renaud, "Impedance spectroscopy flow cytometry: On - chip label - free cell differentiation," *Cytometry Part A*, vol. 65, no. 2, pp. 124-132, 2005.
- [81] T. Sun and H. Morgan, "Single-cell microfluidic impedance cytometry: a review," *Microfluidics and Nanofluidics*, vol. 8, no. 4, pp. 423-443, 2010.
- [82] M.-H. Wang and L.-S. Jang, "A systematic investigation into the electrical properties of single HeLa cells via impedance measurements and COMSOL simulations," *Biosensors and bioelectronics*, vol. 24, no. 9, pp. 2830-2835, 2009.

- [83] S. Gawad, L. Schild, and P. Renaud, "Micromachined impedance spectroscopy flow cytometer for cell analysis and particle sizing," *Lab on a Chip*, vol. 1, no. 1, pp. 76-82, 2001.
- [84] Y. Xu, X. Xie, Y. Duan, L. Wang, Z. Cheng, and J. Cheng, "A review of impedance measurements of whole cells," *Biosensors and Bioelectronics*, vol. 77, pp. 824-836, 2016.
- [85] J. Chen, C. Xue, Y. Zhao, D. Chen, M.-H. Wu, and J. Wang, "Microfluidic impedance flow cytometry enabling high-throughput single-cell electrical property characterization," *International journal of molecular sciences*, vol. 16, no. 5, pp. 9804-9830, 2015.
- [86] J. McGrath, C. Honrado, D. Spencer, B. Horton, H. Bridle, and H. Morgan, "Analysis of parasitic Protozoa at the single-cell level using microfluidic impedance cytometry," *Scientific reports*, vol. 7, no. 1, p. 2601, 2017.
- [87] K. Ahuja *et al.*, "Toward point-of-care assessment of patient response: a portable tool for rapidly assessing cancer drug efficacy using multifrequency impedance cytometry and supervised machine learning," *Microsystems & Nanoengineering*, vol. 5, no. 1, p. 34, 2019.
- [88] D. Holmes *et al.*, "Leukocyte analysis and differentiation using high speed microfluidic single cell impedance cytometry," *Lab on a Chip*, vol. 9, no. 20, pp. 2881-2889, 2009.
- [89] N. Haandbæk, S. C. Bürgel, F. Heer, and A. Hierlemann, "Characterization of subcellular morphology of single yeast cells using high frequency microfluidic impedance cytometer," *Lab on a Chip*, vol. 14, no. 2, pp. 369-377, 2014.
- [90] Y. Song *et al.*, "Capacitive detection of living microalgae in a microfluidic chip," *Sensors and Actuators B: Chemical*, vol. 194, pp. 164-172, 2014.
- [91] R. o. A. Resistance, *Tackling drug-resistant infections globally: final report and recommendations*. Review on antimicrobial resistance, 2016.
- [92] R. V. Milani, J. K. Wilt, J. Entwisle, J. Hand, P. Cazabon, and J. G. Bohan, "Reducing inappropriate outpatient antibiotic prescribing: normative comparison using unblinded provider reports," *BMJ open quality*, vol. 8, no. 1, 2019.
- [93] P. Athamanolap, K. Hsieh, L. Chen, S. Yang, and T.-H. Wang, "Integrated bacterial identification and antimicrobial susceptibility testing using PCR and high-resolution melt," *Analytical chemistry*, vol. 89, no. 21, pp. 11529-11536, 2017.
- [94] C. Cuny and W. Witte, "PCR for the identification of methicillin-resistant *Staphylococcus aureus* (MRSA) strains using a single primer pair specific for SCCmec elements and the neighbouring chromosome-borne orfX," *Clinical microbiology and infection*, vol. 11, no. 10, pp. 834-837, 2005.
- [95] M. Espy *et al.*, "Real-time PCR in clinical microbiology: applications for routine laboratory testing," *Clinical microbiology reviews*, vol. 19, no. 1, pp. 165-256, 2006.
- [96] A. Huletsky *et al.*, "New real-time PCR assay for rapid detection of methicillin-resistant *Staphylococcus aureus* directly from specimens

- containing a mixture of staphylococci," *Journal of clinical microbiology*, vol. 42, no. 5, pp. 1875-1884, 2004.
- [97] J. D. Lutgring, C. Bittencourt, E. M. TeKippe, D. Cavuoti, R. Hollaway, and E. M. Burd, "Evaluation of the Accelerate Pheno system: results from two academic medical centers," *Journal of clinical microbiology*, vol. 56, no. 4, 2018.
 - [98] L. B. Reller, M. Weinstein, J. H. Jorgensen, and M. J. Ferraro, "Antimicrobial susceptibility testing: a review of general principles and contemporary practices," *Clinical infectious diseases*, vol. 49, no. 11, pp. 1749-1755, 2009.
 - [99] J. Barenfanger, C. Drake, and G. Kacich, "Clinical and financial benefits of rapid bacterial identification and antimicrobial susceptibility testing," *Journal of clinical microbiology*, vol. 37, no. 5, pp. 1415-1418, 1999.
 - [100] S. Emaminejad, M. Javanmard, R. W. Dutton, and R. W. Davis, "Microfluidic diagnostic tool for the developing world: Contactless impedance flow cytometry," *Lab on a Chip*, vol. 12, no. 21, pp. 4499-4507, 2012.
 - [101] O. A. Saleh and L. L. Sohn, "An artificial nanopore for molecular sensing," *Nano letters*, vol. 3, no. 1, pp. 37-38, 2003.
 - [102] O. Saleh and L. Sohn, "Quantitative sensing of nanoscale colloids using a microchip Coulter counter," *Review of Scientific Instruments*, vol. 72, no. 12, pp. 4449-4451, 2001.
 - [103] O. Saleh and L. Sohn, "Correcting off-axis effects in an on-chip resistive-pulse analyzer," *Review of scientific instruments*, vol. 73, no. 12, pp. 4396-4398, 2002.
 - [104] A. Carbonaro and L. Sohn, "A resistive-pulse sensor chip for multianalyte immunoassays," *Lab on a Chip*, vol. 5, no. 10, pp. 1155-1160, 2005.
 - [105] J. Sui, P. Xie, Z. Lin, and M. Javanmard, "Electronic classification of barcoded particles for multiplexed detection using supervised machine learning analysis," *Talanta*, p. 120791, 2020.
 - [106] H. Song *et al.*, "A microfluidic impedance flow cytometer for identification of differentiation state of stem cells," *Lab on a Chip*, vol. 13, no. 12, pp. 2300-2310, 2013.
 - [107] H. C. Koydemir *et al.*, "A survey of supervised machine learning models for mobile-phone based pathogen identification and classification," in *Optics and Biophotonics in Low-Resource Settings III*, 2017, vol. 10055, p. 100550A: International Society for Optics and Photonics.
 - [108] H. C. Koydemir *et al.*, "Rapid imaging, detection and quantification of Giardia lamblia cysts using mobile-phone based fluorescent microscopy and machine learning," *Lab on a chip*, vol. 15, no. 5, pp. 1284-1293, 2015.
 - [109] Y. Zuo, S. Chakrabartty, Z. Muhammad-Tahir, S. Pal, and E. C. Alocilja, "Spatio-temporal processing for multichannel biosensors using support vector machines," *IEEE Sensors Journal*, vol. 6, no. 6, pp. 1644-1651, 2006.
 - [110] J. Guo, Z. Chen, Y.-L. Ban, and Y. Kang, "Precise enumeration of circulating tumor cells using support vector machine algorithm on a microfluidic

- sensor," *IEEE Transactions on Emerging Topics in Computing*, vol. 5, no. 4, pp. 518-525, 2017.
- [111] L. Zhang and Y. Zhu, "Dielectrophoresis of Janus particles under high frequency ac-electric fields," *Applied Physics Letters*, vol. 96, no. 14, p. 141902, 2010.
 - [112] A. Irimajiri, T. Hanai, and A. Inouye, "A dielectric theory of "multi-stratified shell" model with its application to a lymphoma cell," *Journal of theoretical biology*, vol. 78, no. 2, pp. 251-269, 1979.
 - [113] A. Valero, T. Braschler, and P. Renaud, "A unified approach to dielectric single cell analysis: Impedance and dielectrophoretic force spectroscopy," *Lab on a Chip*, vol. 10, no. 17, pp. 2216-2225, 2010.
 - [114] A. Bamshad, A. Nikfarjam, M. H. Sabour, and H. Raji, "Theoretical and numerical investigation of liquid-gas interface location of capillary driven flow during the time throughout circular microchannels," in *2017 5th RSI International Conference on Robotics and Mechatronics (ICRoM)*, 2017, pp. 432-438: IEEE.
 - [115] J. Sui, P. Xie, Z. Lin, and M. Javanmard, "Multiplexed molecular biomarker analysis using an expanded library of nanoelectronically barcoded particles enabled through machine learning analysis," in *2018 IEEE Micro Electro Mechanical Systems (MEMS)*, 2018, pp. 444-447: IEEE.
 - [116] J. Mok, M. N. Mindrinos, R. W. Davis, and M. Javanmard, "Digital microfluidic assay for protein detection," *Proceedings of the National Academy of Sciences*, vol. 111, no. 6, pp. 2110-2115, 2014.
 - [117] S. Wang, W. Lambert, S. Giang, R. Goericke, and B. Palenik, "Microalgal assemblages in a poikilohaline pond," *Journal of phycology*, vol. 50, no. 2, pp. 303-309, 2014.
 - [118] F. Foflonker, D. C. Price, H. Qiu, B. Palenik, S. Wang, and D. Bhattacharya, "Genome of the halotolerant green alga *Picochlorum* sp. reveals strategies for thriving under fluctuating environmental conditions," *Environmental microbiology*, vol. 17, no. 2, pp. 412-426, 2015.
 - [119] F. Foflonker *et al.*, "The unexpected extremophile: tolerance to fluctuating salinity in the green alga *Picochlorum*," *Algal Research*, vol. 16, pp. 465-472, 2016.
 - [120] A. Läuchli and U. Lüttge, *Salinity: Environment-plants-molecules*. Springer, 2002.
 - [121] H. Morgan, T. Sun, D. Holmes, S. Gawad, and N. G. Green, "Single cell dielectric spectroscopy," *Journal of Physics D: Applied Physics*, vol. 40, no. 1, p. 61, 2006.
 - [122] W. J. Henley *et al.*, "Phylogenetic analysis of the 'Nannochloris-like' algae and diagnoses of *Picochlorum oklahomensis* gen. et sp. nov. (Trebouxiophyceae, Chlorophyta)," *Phycologia*, vol. 43, no. 6, pp. 641-652, 2004.
 - [123] B. Khraiwesh *et al.*, "Genome-wide expression analysis offers new insights into the origin and evolution of *Physcomitrella patens* stress response," *Scientific reports*, vol. 5, p. 17434, 2015.

- [124] N. Wang, Z. Qian, M. Luo, S. Fan, X. Zhang, and L. Zhang, "Identification of salt stress responding genes using transcriptome analysis in green alga *Chlamydomonas reinhardtii*," *International journal of molecular sciences*, vol. 19, no. 11, p. 3359, 2018.
- [125] M. A. Borowitzka, "The 'stress' concept in microalgal biology—homeostasis, acclimation and adaptation," *Journal of applied phycology*, vol. 30, no. 5, pp. 2815-2825, 2018.
- [126] R. R. Guillard and J. H. Ryther, "Studies of marine planktonic diatoms: I. *Cyclotella nana* Hustedt, and *Detonula confervacea* (Cleve) Gran," *Canadian journal of microbiology*, vol. 8, no. 2, pp. 229-239, 1962.
- [127] P. Kim, K. W. Kwon, M. C. Park, S. H. Lee, S. M. Kim, and K. Y. Suh, "Soft lithography for microfluidics: a review," 2008.
- [128] J. Sui, F. Foflonker, D. Bhattacharya, and M. Javanmard, "Electrical impedance as an indicator of microalgal cell health," *Scientific reports*, vol. 10, no. 1, pp. 1-9, 2020.